Electron Cyclotron Resonance Thruster Diagnostics & Performance Analysis

Lillie A. LaPlace

University of Washington

A thesis

submitted in partial fulfillment of the

requirements for the degree of

Master of Science

University of Washington

2026

Committee:

Justin Little

Uri Shumlak

Program Authorized to Offer Degree:

Aeronautics & Astronautics

University of Washington

Abstract

Electron Cyclotron Resonance Thruster Diagnostics & Performance Analysis

Lillie A. LaPlace

Chair of the Supervisory Committee: Justin Little

This thesis describes the process by which the performance of an electrodeless, coaxial electron cyclotron resonance thruster is evaluated. Using a thrust stand, retarding potential analyzer, and Faraday probe, the performance of the thruster under various permutations of steady state and pulsed operating regimes was analyzed in terms of thrust performance, plasma properties, including ion energy distribution functions, pulse current contour profiles, and thruster plume characteristics, including plume divergence and mass utilization efficiency. Performance for each permutation of pulsed operating regime is evaluated and compared quantitatively using a series of analysis scripts to isolate the thruster's behavior at different time slices throughout a pulse. Operating in a high maximum power pulse regime, with a low average power, could offer a way to leverage improvements in ionization efficiency and mass utilization fraction associated with operating at a high power without the large spacecraft power capacity associated with continuously operating at this high power. These results demonstrate that pulsed operation does not appear to manifest a significant degradation in performance for comparable continuous operational settings relative to average power. However, in comparing between the two pulse regimes assessed, longer duty cycles did correlate with increased overall performance.

Author Note

This thesis was completed with the support of the Space Power and Propulsion for Agility, Responsiveness and Resilience (SPAR) Institute and United States Space Force (USSF). Any opinions, findings, and conclusions or recommendations expressed in this material are those of the author and do not necessarily reflect the views of the SPAR Institute or USSF.

Table of Contents

List of Figures

Acknowledgements

Thank you to my parents for encouraging me to reach for the stars as a kid. I know the five-year-old version of me who was obsessed with black holes and sitting outside with the Dobsonian would be really happy to see how things turn out. Your support made it possible for me to experience what it was like to find my people. There's nothing quite like staring up at the Atlantis orbiter or even the VAB as a 13-year-old and getting overwhelmed with the feeling of wanting to be part of something that big with people who are just as passionate about it as you are. Also, thank you to my favorite sibling, you know who you are.

Merci mamie « Je ne désespère pas de marcher sur la Lune un jour » c'est toujours vrai aujourd'hui ; si j'ai l'occasion d'y aller, tu viendras avec moi. To grandma, thanks for always being there to listen to and support me.

Big thanks to Bennett and Ripu for making this thesis survivable. I cannot stress how nice it was to be able to rant about anything and everything over lunch. I also cannot overstate how valuable both your help and feedback were throughout this endeavor. Shoutout to the rest of the lab for generally being awesome as well.

To both grandpa and papi: you're not going to read this, but just know that I took both of your love for planes and ran with it. Grandpa: I still see parts you developed in many of the projects I've worked on, and I think about you every time I see a Blackbird. To papi: you got to watch dogfights while lying in fields, but were denied a chance to get an education; I like to think that you'd be happy I'm building things that fly now.

Last but certainly not least, thank you to my advisor, Professor Justin Little and to Uri Shumlak. With so many distractions in current events, it's easy to lose sight of what makes this work so meaningful, and I've truly appreciated getting to learn from all of you through my classes and see your passion for your work. To Justin, thank you for supporting me as a researcher. I'm really looking forward to continuing on with my research through a doctorate.

Electron Cyclotron Resonance Thruster Diagnostics & Performance Analysis

Introduction

Electron cyclotron resonance (ECR) thrusters are part of a longstanding progression toward propellant agnostic, electrodeless electric propulsion (EP) thrusters. As this project is intended to

EP systems were first proposed by Robert Goddard in 1906. The fundamental physics of rocket propulsion had long-since been resolved as mathematical exercises, particularly through Tsiolkovsky's seminal work; what remained was the practical implementation of such concepts. Though rocket propulsion advanced considerably in the following decades, EP was not seriously pursued as a means of propulsion until the early 1960s. This work was largely pioneered by the Russian space effort. [1]

Basics of Rocket Propulsion & EP

Konstantin Tsiolkovsky was among the first to propose electric acceleration of particles being used as means for space propulsion, only a few years after his 1903 seminal publication, "Investigation of Universal Space by Means of Reactive Devices," in which he presented his now famous rocket equation:

$$\Delta V = v_e \ln\left(\frac{m_0}{m_f}\right),$$

where ΔV is the change in velocity imparted to a rocket, v_e is the exhaust velocity of propellant, m_0 is the rocket's initial mass, and m_f is the rocket's final mass. [2] This foundational equation establishes two variables for maximizing ΔV: the exhaust velocity and the mass ratio of fueled to unfueled rocket, both of which are to be maximized for maximum ΔV. However, where EP becomes useful with high exhaust velocities, since with a logarithmic dependence on the mass ratio, this variable becomes increasingly less appealing to increase, as returns diminish quickly when the rocket begins to need to be impractically large. Exit velocity is simply calculated from $v_e = I_{sp} g_0$, where I_{sp} is the specific impulse, g_0 is Earth's standard, sea level gravitational acceleration, and $I_{sp} = \frac{F}{\dot{m} g_0}$. It can be seen within this equation that specific impulse is essentially a ratio of thrust produced to mass flow rate, meaning that it can be optimized Tsiolkovsky had recognized this, and noted that “It is possible that in time we may use electricity to produce a large velocity for the particles ejected from a rocket device.” [2]

In 1920, Dr. Robert Goddard was granted the first patent for an electric thruster after he’d pioneered electric propulsion concepts starting with a publication in 1906. The theory behind electric propulsion was long-since established before any serious complementation of its implementation was considered. In the 1950s, Ernst Stuhlinger, a physicist brought to the United States from Germany as part of Operation Paperclip, began working on electric propulsion research as a side hobby to his assigned work on US missile guidance systems. He eventually published “Ion Propulsion for Space Flight,” in 1964, a book still heavily referenced in EP publications today. Taken together, these works illustrate that the foundational physics of much of the electric propulsion systems in use today were largely established in the past century. The great difficulty with electric propulsion systems has been their practical implementation rather than any theoretical limitations on their operation.

The first electric propulsion systems to fly and operate successfully were designed and built by the Soviet Union. Soviet scientists pioneered electromagnetic propulsion systems like pulsed plasma thrusters and Hall thrusters throughout the 1960s and deployed them into orbit. The United States had primarily focused its EP research efforts into gridded ion thrusters during this time period. It wasn’t until the 1990s, after the collapse of the USSR, that this technology began to be used and developed by other countries like the United States and France. [3]

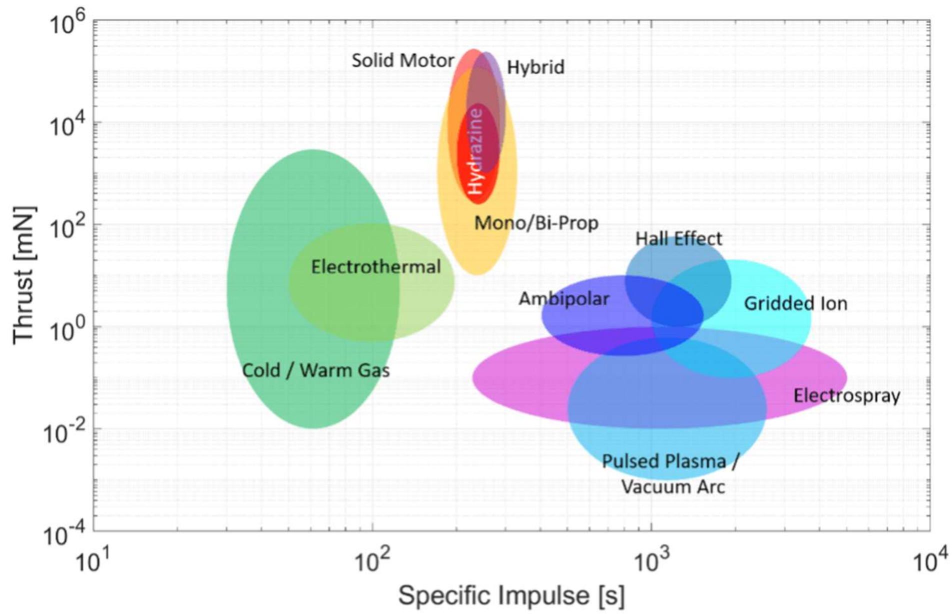

Figure 1: Thrust vs. Specific Impulse for In-space Propulsion Systems (NASA)

Contemporary ECR Research Efforts

Relative to other EP concepts, in practice, ECR thrusters are in their infancy and have not been flown in any known operational space vehicles. The theory behind their operation has long-since been established, so the primary challenges today lie in their engineering and operations. In Figure 1: Thrust vs. Specific Impulse for In-space Propulsion Systems (NASA) above, ECR thrusters typically fall within the high specific impulse, low thrust regime, with the best currently reported thrust performance sitting at 3.1 mN and approximately 900 s of specific impulse, from France's Office National d'Études et de Recherches Aérospatiales (ONERA) research group. [4]

ECR thrusters have previously been investigated within the SPACE Lab as part of efforts to characterize molecular propellant performance, as electrodeless thrusters are inherently more versatile in terms of propellant compatibility and lifetime constraints relative to thrusters featuring electrodes. Most recently, Sheppard assessed the performance of using water as a propellant with an insulated antenna and axial propellant injection design. [5] Though this thesis focuses on assessing krypton performance, a multispecies molecular propellant, ASCENT, was also tested and assessed, building off Sheppard's work.

SPAR Project Overview & Multimodal Propulsion

The Space Power and Propulsion for Agility, Responsiveness and Resilience (SPAR) Institute aims to provide the United States Space Force with a propulsion architecture for a nuclear-powered spacecraft with both chemical propulsion and EP systems, for high and low thrust maneuvering, respectively. These power systems would operate using a common propellant compatible with both combustion and ionization. A goal of this architecture is to select an EP system capable of delivering high specific impulse, reliable propulsion for stationkeeping and long-duration orbital maneuvering.

An important part of this architecture is testing the use of a hydrocarbon-based propellant capable of generating thrust in both chemical propulsion and EP systems. While several propellants' performances were evaluated throughout multiple test campaigns for this thruster, including a combustion product simulant of ASCENT, a high density, "green" monopropellant developed by the Air Force Research Laboratory (AFRL), due to the sensitive nature of such a propellant's performance data, this thesis centers on the analysis of the thruster's operation using krypton propellant alone. Krypton was selected for its widespread use in currently operating satellites, ready availability of published performance data from other thrusters, ease of procurement, and favorable performance.

The University of Washington's Space Propulsion and Advanced Concepts Engineering Laboratory (SPACE Lab) was tasked with evaluating the performance of an ECR thruster initially designed by the University of Michigan's (UM) Plasma Dynamics and Electric Propulsion Laboratory (PEPL). UM's thruster design was derived from ONERA's ECR-PM-V1 coaxial ECR thruster. [6] The ECR-PM-V1 has been used as a basis for ECR testing and characterization at both UM and UW throughout several test campaigns. [5] [7]

Following initial receipt of the thruster, various modifications to the thruster's design have been made. These modifications include redesigning the antenna connector, evaluating impacts on performance from anodizing several thruster components, and assessing changes in performance with the implementation of a metallic nozzle. Building off an initial low power characterization of this thruster design, future work for SPAR project work within the SPACE Lab includes designing and testing a high power ECR thruster, drawing on lessons learned from this low power thruster's performance characterization and any testing bottlenecks noted, as described within this thesis.

ECR Thruster Fundamentals

An ECR thruster operates off two driving phenomena. The first is the acceleration of electrons through a monopole antenna, generating a linearly oscillating electric field along the longitudinal axis of the thruster at the frequency of the supplied power. The second is the rotational motion of electrons in a magnetic field, dictated by the electron gyrofrequency equation:

$$\omega_{ce} = \frac{eB}{m_e},$$

where e is an electron's fundamental charge, B is the strength of the magnetic field at which an electron is located, and m_e is an electron's mass. In a magnetic field, charged particles follow curved paths due to the Lorentz force. The force generated by a charged particle moving through a magnetic field is such that it is perpendicular to its velocity and magnetic field vectors, given by the following equation:

$$F = q(v \times B),$$

where q is the particle's charge, v is its velocity, and B is the magnetic field vector. As a particle's velocity and or the surrounding magnetic field change, the force generated must always remain perpendicular. For a particle traveling through a fixed magnetic field, the velocity must continuously change to maintain orthogonality to the magnetic field, generating a circular motion about the field lines analogous to a centripetal force. [8]

At a high level, resonance is achieved with the synchronization of the frequency of electron oscillation in the monopole antenna with the cyclotron frequency of the electrons in the magnetic field. As electrons are lighter than ions, and are therefore more readily displaceable, the energy deposited into them by both the antenna and magnet gives them sufficient kinetic energy to eject from the thruster. As the electrons separate from the ions that remain within the ECR region of the thruster, they generate a potential field that then accelerates the ions out of the thruster.

Plasma Physics Fundamentals

A plasma is generally defined as an ionized, but bulk neutral, gas that displays collective behavior. It is primarily governed by electromagnetic interactions rather than collisions. Broadly speaking, plasmas vary significantly in behavior depending on their number density and applied magnetic field strength. This relationship is often expressed in terms of the plasma frequency, a function of electron density, given by:

$$\omega_{pe} = \sqrt{\frac{ne}{\epsilon_0 m_e}}$$

where n is electron number density, e is electron fundamental charge, ϵ_0 is the permittivity of free space, and m_e is the mass of an electron, and by electron cyclotron frequency, with both expressed as ratios of wave frequency within the plasma. Electron density, n, is on the order of 10E17 $[m^{-3}]$ on the lower end of what's typical for an ECR thruster plume at 3 sccm volumetric ideal gas flow and 100 W operating power, yielding a ω_{pe} on the order of 10E19 $[Hz]$. [9]

This relationship is characterized in the Clemmow-Mullaly-Allis (CMA) diagram illustrated below in Figure 2: CMA Diagram. The CMA diagram is derived from the Cold Plasma Dispersion Relation (CDPR), which includes several limiting assumptions, most evident of which, is that of a cold, nonthermal plasma. ECR thrusters primarily operate through exciting electrons and subsequently accelerating ions; they do not directly heat ions, therefore this is a valid assumption to make.

For the purposes of this ECR thruster, the plasma generated within the ECR region is situated in Region 8b of the CMA diagram. At exactly the electron cyclotron resonance frequency, $\omega = \omega_{ce}$, this corresponds to the horizontal line in Figure 2: CMA Diagram below at $\frac{|\Omega_e|}{\omega} = 1$. However, parts of the thruster's operation are better described such that $\omega \leq \omega_{ce}$, while the electron plasma frequency ω_{pe} is assumed to be much larger than the frequency of the input signal, as the input signal is on the order of 10E9

$[Hz]$. In this region, only the R wave will propagate through the plasma, while other types will be cut off due to the plasma being opaque to them.

The R wave is known as the right hand circularly polarized (RHCP) wave, or in more space plasma-oriented literature, as the Whistler wave. Unlike the left hand circularly polarized (LHCP) wave, which opposes the direction of the gyrating electrons within the magnetic field relative to the direction of propagation and is present in Region 7, this RHCP wave propagates forward with the same rotational orientation as the gyrating electrons.

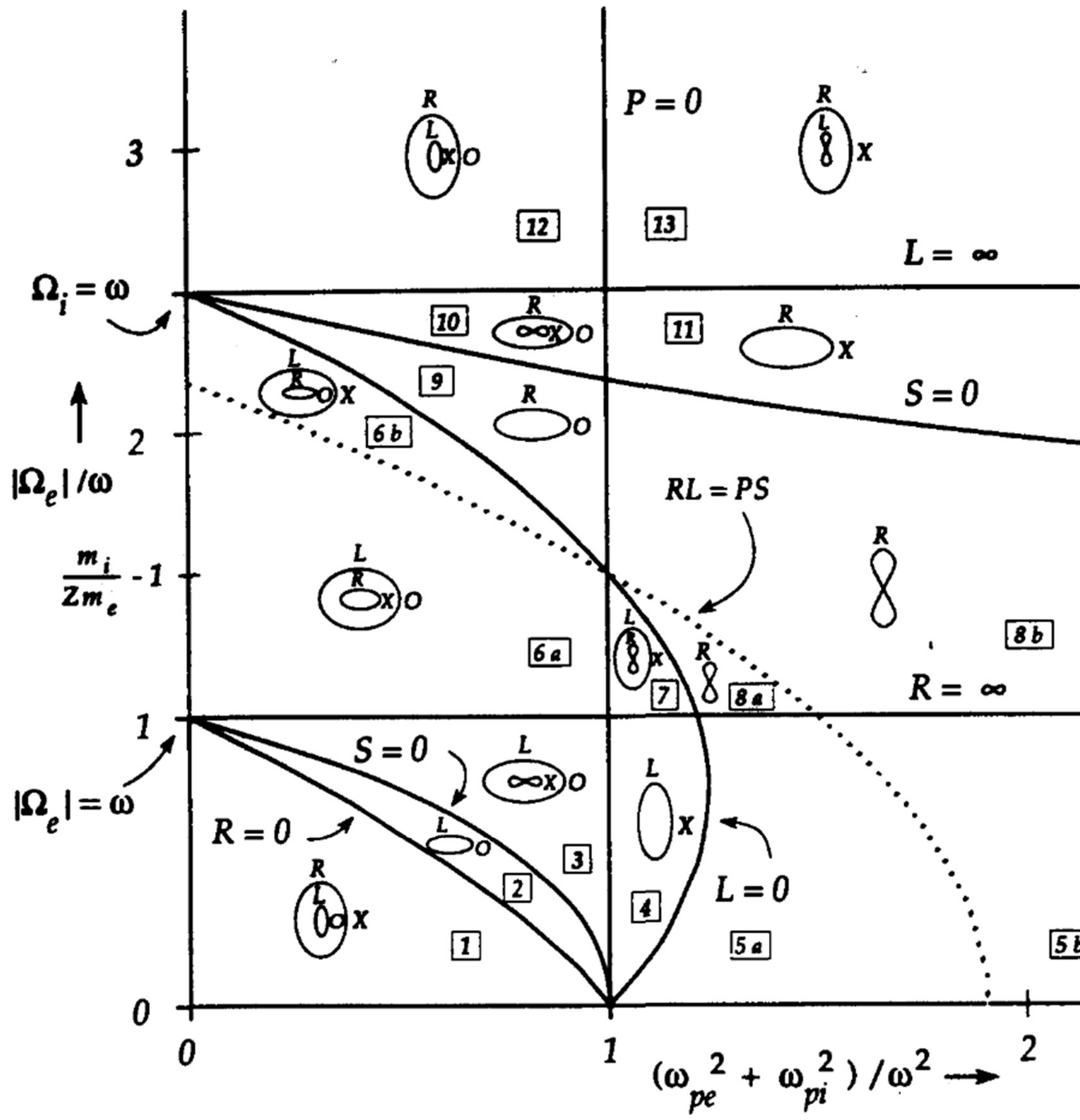

Figure 2: CMA Diagram [10]

ECR Thruster Theory of Operation

A monopole antenna functions by receiving current from a source and converting it into radio waves that emit outward in an approximately toroidal flux pattern with respect to its longitudinal axis that is bisected at the ground plane. The coaxial connector's outer shielding functions as a ground in this application. From transmission line theory, maximum power is emitted radially at some angle above the horizontal, with zero power is emitted from the endpoint, as all power is reflected into the antenna.

In the thruster evaluated for this campaign, as designed, the antenna approximately functions as a half-wave monopole. Gain is higher than with a more conventional quarter-wave monopole and the resulting half power beamwidth (HPBW) is narrower, meaning that power is radiated at a higher density within the ECR region surrounding the antenna azimuthally. Under ideal conditions, HPBW for such an antenna is 24° (3dB E-plane) and the antenna's maximum gain is 6.82 dBi. [11]

At a high level, the thruster operates as follows: current is supplied to the antenna through a radiofrequency (RF) power source set to a single frequency. The current accelerates electrons in the antenna linearly in an oscillating motion back and forth along the longitudinal axis. At first, this electron motion within the antenna generates an oscillating electric field and linearly polarized waves. These linearly polarized waves accelerate electrons within the neutral gas, but because this process occurs in a magnetized region, thanks to the thruster's permanent magnet surrounding the ECR region, a Lorentz force is generated and the electrons begin to adopt counterclockwise circular paths. A transition occurs between the initial linear oscillation of the electrons and their eventual circular paths due to collisional processes.

At a high level, this linearly polarized electric field ultimately deposits energy into the gas supplied to the thruster by means of plasma resonances, with the plasma itself generating circularly polarized waves, when this process occurs in a magnetized region. More granularly, within an ECR thruster's plasma regime, only the R wave can propagate. The R wave propagates parallel to the magnetic field, facilitating the acceleration and ejection of electrons from the thruster. The O, X, and L waves do not contribute to the formation of a plasma, as they are all cut off and do not propagate within the 8a region of the CMA diagram. [12]

This thruster operates by injecting neutral gas propellant radially into the ionization region surrounding the antenna. As the antenna's electric field oscillates, it deposits energy into the gas by means of the linearly polarized waves accelerating a small number of free "seed electrons" already present in the gas. These "seed electrons" kinetically impact surrounding neutrals following their acceleration by the monopole antenna and release more electrons, which then become free to interact with other neutrals and release an increasing number of electrons through collisional processes. The energy at which these collisions lead to the ionization of neutral species is at minimum, the binding energy of a valence shell electron. Because the collisional cross section for these electron impacts is at its minimum when the kinetic energy of the impinging electrons matches with the binding energy, an ECR process is most efficient when the kinetic energy is 2-3 times the magnitude of the binding energy, as collisional cross section is at its maximum for this condition. [13]

Therefore, as gas flows into the chamber and energy is deposited into the atoms' electron energy states thanks to the RF power supplied, these particles become ionized through direct impact ionization from free electrons. During this process, electrons collide with neutral species, free up more electrons, and drive further ionization. However, ions also become neutralized due to charge exchange interactions with neutrals. The balance of impact ionization and charge exchange neutralization is modeled as follows to yield the overall 0-dimensional ion charge state distribution:

$$\frac{\partial n_i}{\partial t} = \sum_{j=j_{\min}}^{i-1} n_e n_j \langle \sigma_{j\to i}^{EI} v_e \rangle + n_0 n_{i+1} \langle \sigma_{i+1\to i}^{CE} v_{i+1} \rangle - n_0 n_i \langle \sigma_{i\to i-1}^{CE} v_i \rangle - \sum_{j=i+1}^{j_{Fmax}} n_e n_j \langle \sigma_{i\to j}^{EI} v_e \rangle - \frac{n_i}{\tau_i},$$

where n_i and n_e are the ion and electron densities at a charge state i, σ represents the cross section for a species in a particular process, and τ_i is the confinement time of the ion within the plasma. [13] When the rate of ion production is zero, the impact ionization and charge exchange interactions are balanced.

The thruster's magnetic field subsequently causes these charged particles to begin to gyrate with cyclotron motion. The lighter, and therefore more mobile, electrons are the first to be acted upon by such a field. The magnetic field strength is tuned such that the electron cyclotron frequency generated by the magnet matches with the RF power frequency supplied to the antenna, generating a resonance. This cyclotron resonance effectively facilitates the conversion of kinetic energy from linear oscillations into gyrating, perpendicular motion along magnetic field lines that drives particle motion out of the thruster.

As the electrons gain energy, they are directed along the magnetic field lines acting as a diverging nozzle past the end plane of the magnet. The field lines act as guiding centers for the electrons. As the nozzle diverges, the electrons' gyrokinetic energy is converted into translational kinetic energy due to conservation of electron energy and magnetic moment. [14] Conservation of energy is such that:

$$\frac{dW}{dt} = 0 = \frac{d}{dt}\left(\frac{1}{2}mv_{\parallel}^{2}\right) + \frac{d}{dt}\left(\frac{1}{2}mv_{\perp}^{2}\right) = -\frac{\mu d\left|\vec{B}\right|}{dt} + \frac{d}{dt}\left(\mu\left|\vec{B}\right|\right),$$

meaning that for a system in which the magnetic moment μ is invariant and the magnetic field strength is constant in time, the rate of change of parallel and perpendicular kinetic energies must be equal and opposite. [15] Because the magnetic moment is given by the following equation, $\mu = \frac{-\frac{1}{2}mv_{\perp}^{2}}{B}$, this means that for it to remain constant as magnetic field decreases with distance from the magnet, perpendicular velocity must similarly decrease. Given that the time integrated form of the equation above is $W = \frac{1}{2}mv_{\parallel}^{2} + \frac{1}{2}mv_{\perp}^{2}$, this means that parallel velocity will increase to offset decreases in the kinetic energy contribution from perpendicular velocity, meaning that the nozzle will effectively convert electrons' rotational motion into translational motion.

The ions are initially less mobile due to their larger mass relative to electrons. However, a charge separation develops between the expelled electrons and remaining ions within the ECR region of the thruster, which then electrostatically accelerates the ions out of the thruster to reduce this potential and attempt to drive the system toward equilibrium. As the ions and electrons are then expelled, together they generate an equal and opposite force that pushes back against the thruster, generating thrust.

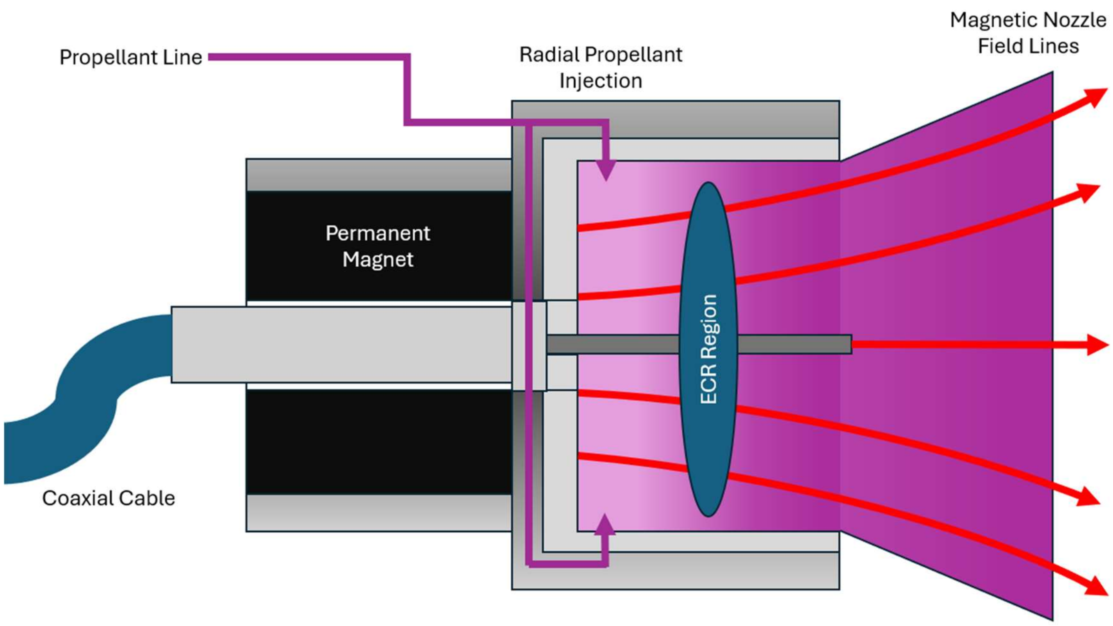

Figure 3: Magnetic Nozzle and ECR Region Configuration

Thruster design

The thruster consists of an aluminum body, TNC adapter and graphite antenna, and boron nitride lining. For a 2.45 GHz ECR thruster, the magnetic field strength required is simply obtained from the electron cyclotron frequency equation as 875 G. For this thruster, this axial field strength is generated by a permanent ring magnet housed behind the antenna. Power is supplied to the thruster through a TNC connector with an adapter onto which a graphite antenna is friction fit. The graphite antenna is concentric to a boron nitride plasma liner into which the propellant injection manifold is integrated. Propellant is fed into the plasma channel by means of radial injection holes at the base of the boron nitride walls. All aforementioned components are housed within an aluminum body that is electrically isolated from the test stand mounting system by means of dielectric standoffs. The thruster assembly CAD, mounted to its backplate, is illustrated below in Figure 4: Thruster Assembly CAD.

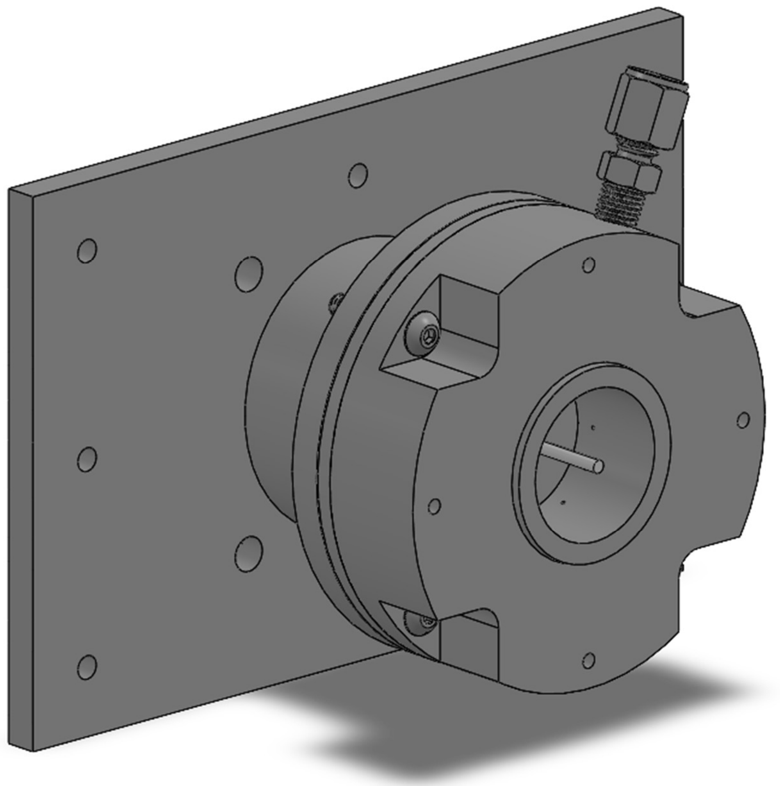

Figure 4: Thruster Assembly CAD

After a string of TNC failures, a thermal standoff was designed to interface with the coaxial cable instead. The primary failure mechanism of the TNC connectors used was the thermal breakdown and sublimation of the PTFE insulation within the connector. During sustained operation, the thruster's antenna undergoes significant heating, to the point that it persistently glowed red hot (Figure 5: Antenna Glow Post-testing for several seconds after thruster operation ceased. This damage is illustrated below in Figure 6: TNC Char Buildup from PTFE Ablation.

Figure 5: Antenna Glow Post-testing

Figure 6: TNC Char Buildup from PTFE Ablation

These TNC failures presented a significant testing bottleneck. Each failure required stopping all testing, returning the chamber to atmospheric pressure, disassembling the thruster, replacing the TNC, reinstalling the thruster, recalibrating the test stand, and then returning the chamber to operational pressure. The thermal standoff shown below in Figure 7: Redesigned Connector (Pink & White) was therefore designed using a machined, boron nitride tube to act as a coaxial connector to the antenna. A tungsten electrode was fitted into the boron nitride, while aluminum tape was used to wrap the outside of the standoff as an outer conductor.

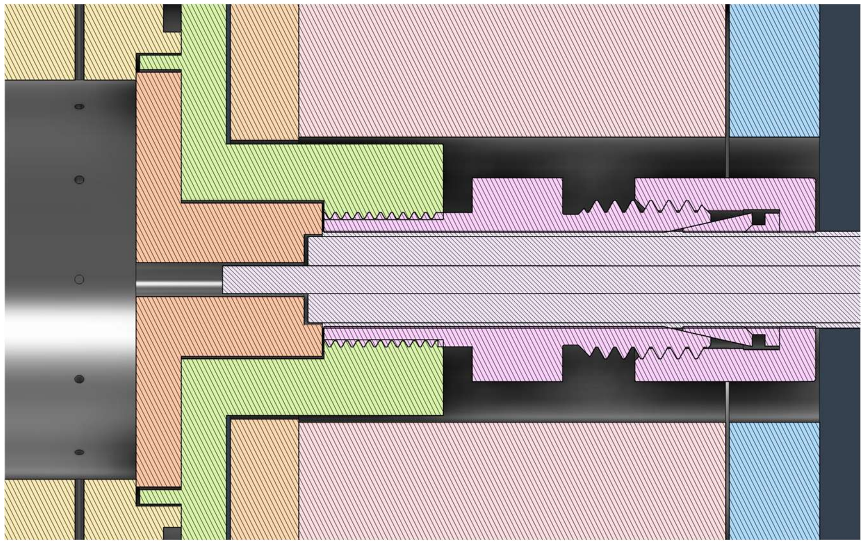

Figure 7: Redesigned Connector (Pink & White)

To ensure that the graphite antenna remained in place during thruster operation, the tungsten electrode used in the modified thermal standoff also featured a 45° cut, with all further antennas similarly cut at 45° at their end to increase the surface contact area and improve the friction fitting. An issue identified during earlier testing was that as the thruster operated for extended periods of time and the antenna experienced some ablation when operating at high powers that resulted in a marginally decreased diameter. This ablation eventually caused the antenna to come loose and be ejected by the gas pressure exerted on it by the propellant injectors. However, after implementing this thermal standoff and 45° cut on the antenna, no further failures occurred, and the antenna remained securely in place throughout the remainder of the test campaign.

Test Facility Overview

All thruster testing was completed in the SPACE Lab's Space Test Facility (STF). This chamber has an internal volume of 3.5 m^3 and maximum krypton pumping speed of 26 kL/s with its turbopump and two cryopumps operating. [16] The chamber is equipped with a linearly actuating platform on which diagnostics can be installed to measure properties at the center of the thruster's plume. It also features a radial armature equipped with a stepper motor that provides a 180 degree sweep of the thruster's plume at a fixed distance of 0.54 m.

To reach operational chamber pressures on the order of 1E-6 Torr, the chamber uses a series of pumps to progressively decrease pressure. A roughing pump consisting of an Emod VUF112/2-110 and Marathon Electric motors driving a RUVAC WSU 501 wet roughing pump pulls vacuum through a gate valve prior to the chamber reaching -60 kPa relative to atmosphere. After this, the Agilent IDP16 dry scroll pump is turned on and a valve between the scroll pump and the Shimadzu TMP-V2304LMP turbopump is opened. This allows for the pressure in the turbopump to drop faster so that it can begin rotating and levitating sooner. The turbopump is turned on once absolute pressure has reached 250 mTorr. When the turbopump has reached its operating rotational speed and a chamber pressure of 50 mTorr is reached, the roughing pump's gate valve is closed, its vent is opened, and the pump itself is turned off. Once a pressure of 20 mTorr or below has been reached, the gate valves for the two R Marathon CP-20 cryopumps are opened one at a time, and testing begins once the chamber pressure stabilizes. After a pressure lower than 1 mTorr is reached, an ion gauge can be turned on as additional pressure monitoring.

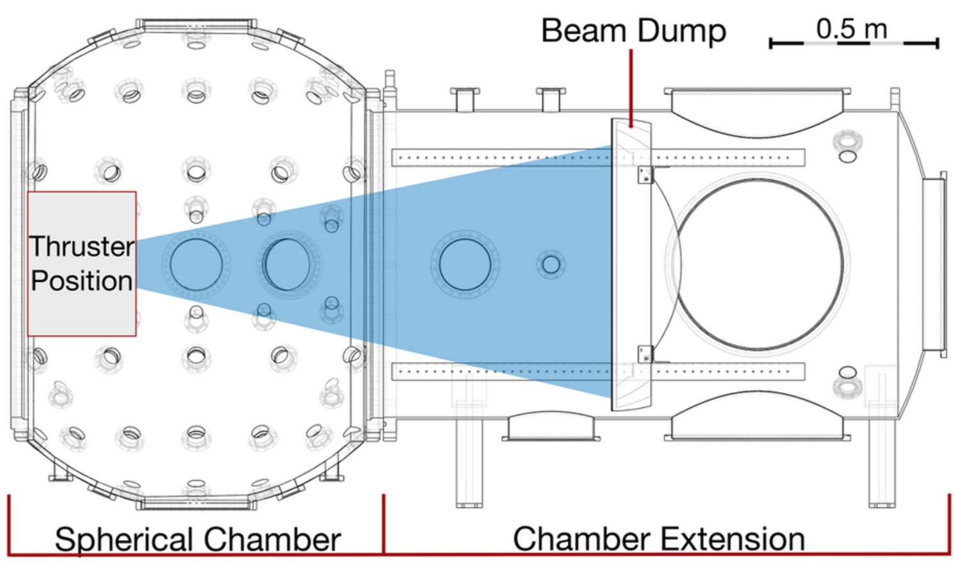

Figure 8: STF Vacuum Chamber [17]

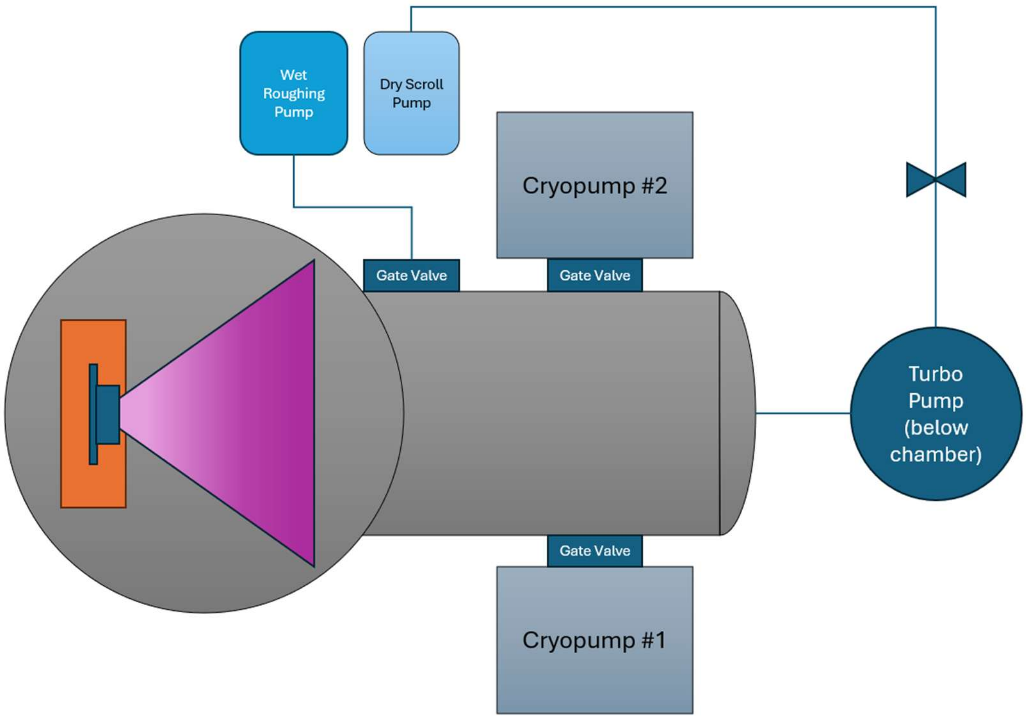

Figure 9: STF Chamber Pump Configuration

Thruster integration

The thruster was mounted to a double inverted pendulum thrust stand with an aluminum extrusion arm. To ensure the thruster remained electrically floating, nylon bolts and nuts passing through ceramic standoffs were used in the interface between the thruster's backplate and the aluminum extrusion arm. The thrust stand uses Keyence IL-100 laser at 655 nm and IL-1000 rangefinder, and features a water-cooled thermal sheath. The inverted pendulum's flexures can be replaced to accommodate thrusters producing between 100 µN and 100 mN, and in the April test campaign, were set to a thickness of 0.0020”. [17]

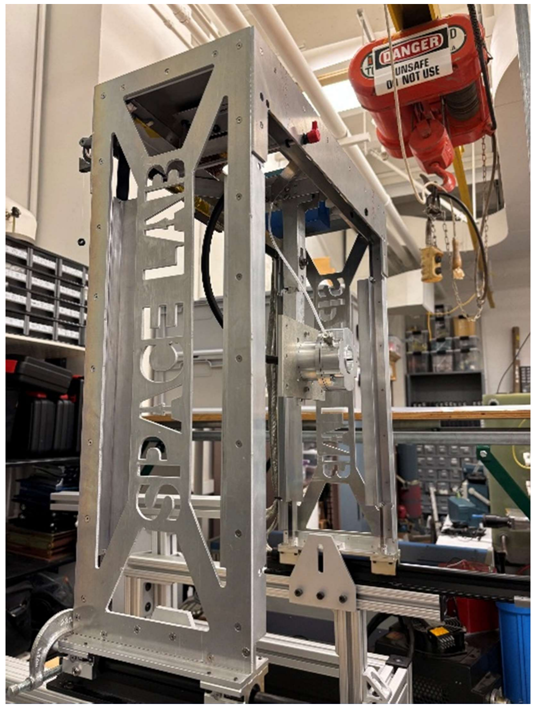

Figure 10: ECR Thruster Integrated onto Thrust Stand

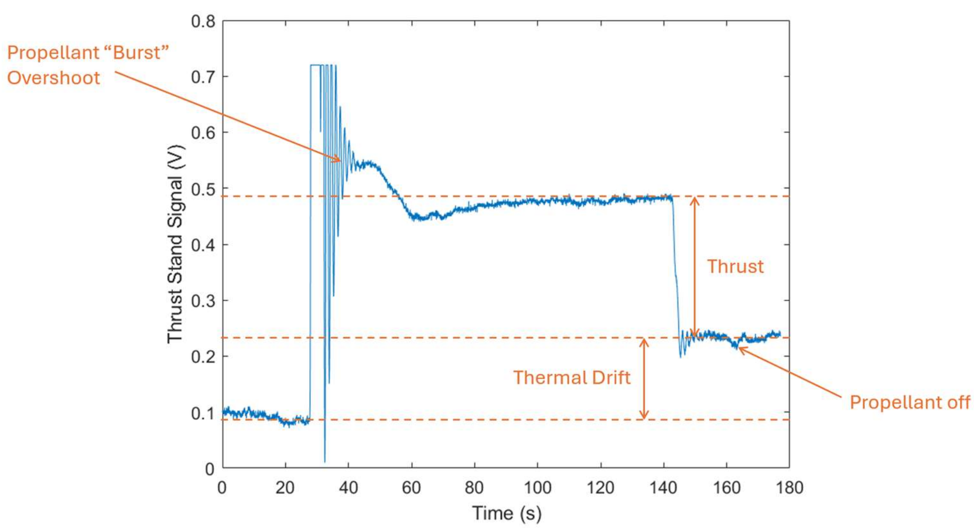

Figure 11: Typical Thrust Stand Response

The thrust stand is calibrated using a small, known mass raised and lowered by an integrated stepper motor. As the mass is moved, it applies a small force that deflects the stand enough to be measured by the rangefinder. The rangefinder's signal is then offset to ensure that throughout the mass's movement, the deflection measured does not exceed the rangefinder's measurement limit. Once the full signal is captured, the change in voltage between the mass being raised and lowered is measured on an oscilloscope, and used to establish a ratio between the voltage associated with the representative thrust produced by the mass and the thrust measurements taken by the thruster.

In each test, the propellant was backfilled in the feedline to "burst" the propellant just as the power supply was turned on. This causes the voltage signal to overshoot and requires that the signal dampens out prior to any accurate characterization of the thruster's behavior in its operation. Thrust is measured once the signal has stabilized after the mass flow rate is set to the value defined for a particular test point, where the oscilloscope's cursor is used to measure the voltage change between the thruster and propellant being on and off. The potential associated with the thruster being off prior to and after testing is typically not identical, as thermal drift causes the potential to trend upward over time, as illustrated in Figure 11: Typical Thrust Stand Response above.

For the thrust stand to be able to deflect with minimal mechanical interference, power is delivered to the thruster from a coaxial cable interfacing with the vacuum chamber to two waveguides. These waveguides are positioned toward each other such that losses during stand deflection are minimized. Once power is transferred across the waveguides, it is again transmitted using an SPP-375LL coaxial cable to the thruster.

A Sairem GMS450 RF power supply was used to supply power to the thruster. This supply could be programmed to generate both steady state at a given power and frequency, and pulsed power, with the option to set frequency, pulse period, length, low, and high power, with its maximum output power setting being 450 W. A SPP-375LL coaxial cable was connected from the Sairem to a dual-directional coupler (DDC), upon which two Keysight U2001B power meters were connected to measure the forward and reflected power. The DDC was connected to a vacuum feedthrough with another coaxial cable. A third coaxial cable connected the feedthrough to the thrust stand's first waveguide within the vacuum chamber. From the second waveguide, power was finally deposited into the thruster through the third SPP-375LL coaxial cable with a TNC adapter to mate with the thruster's TNC connector.

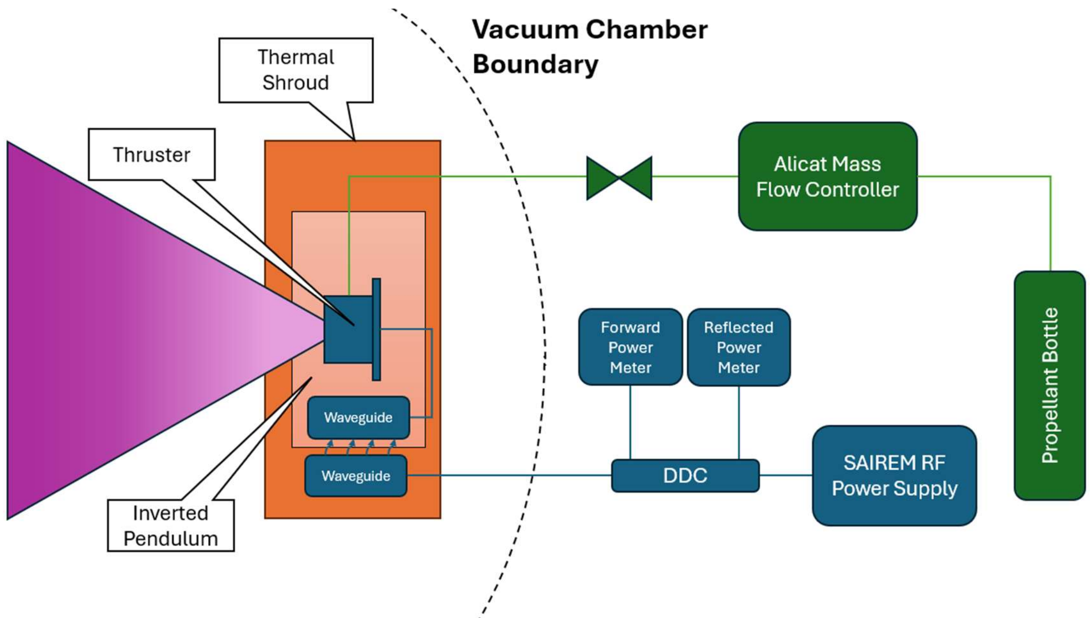

Figure 12: Thruster Power and Gas Feed Systems

The loss through the power system was characterized by measuring the forward and reflected power using a Keysight U2001B power meter at the thruster following every removal and reinstallation of the thrust stand into the chamber. Prior to beginning testing in earnest, the power system was successively tested with the addition of one more component each time to characterize each component's reduction in power gain. On average, the total forward power conversion loss was 1.31 dB from the Sairem to the thruster's TNC.

Gas was supplied to the thruster through the thrust stand by a waterfalled Tyvek tube within the vacuum chamber. All external piping was metallic to minimize leakage. Flow to the thruster was set and regulated by an Alicat 2.5 SLPM mass flow controller with a manual valve at the chamber feedthrough. This manual valve was closed as the mass flow was set to a given test point, which allowed for the accumulation of gas within the feedline to "burst" propellant as the power supply was turned on to increase propellant density for more consistent plasma ignition.

Diagnostics

Overview

Diagnostics were selected to introduce minimal perturbations to the thruster's operation while collecting data on quantities of interest. Ultimately, a swept Faraday probe (FP) and retarding potential analyzer (RPA) set at a fixed point downstream of the thruster were implemented. The swept FP provides both temporally and spatially resolved ion current measurements, while the RPA provides time resolved ion current measurements over a sweep of voltages to characterize the distribution of ion energy populations within the thruster plume.

Faraday Probe Theory

A Faraday probe operates by biasing a collector and concentric guard ring to a particular voltage, onto which incident particles are directed. This bias voltage generates a current between the ions within the thruster plume and the collector electrode. To minimize plasma sheath effects, a guard ring is also employed, separated from the collector by a small gap and biased to the same voltage as the collector; it effectively "smooths out" the sheath surrounding the collector to create a flatter, more uniform sheath. [18] It is primarily used to characterize ion flux and plume divergence downstream of the thruster.

For this campaign, the FP was used to generate a high-resolution plot of the pulse's geometry in both space and time. The FP was also used to calculate mass utilization and plume properties including divergence and full width half maximum (FWHM).

The FP used for these experiments was mounted on a 180° sweeping arm within the vacuum chamber at a radius of 0.54 m from the thruster's exit plane. The probe has a diameter of 12.5 mm and features a guard ring with a diameter of 24 mm, and a gap between the probe and guard ring's inner diameter of 0.4 mm. The probe was constructed from 0.5 mm thick 99.9% molybdenum backed with electrically isolated alumina silicate that interfaced with the swept arm onto which the probe was mounted. The FP operated using a TDK-Lambda GEN600-1.3 power supply to bias both the probe and guard ring to the same voltage. The current across the probe was measured using a 1072 Ω resistor. [5]

A custom opto-isolated transimpedance amplifier (TIA) was designed and implemented to ensure that measurements could reliably be taken from the Faraday probe regardless of the potential at which the amplifier operates. The primary concern was that the floating potential of the probe could be high relative to the ground and introduce common-mode noise to the probe circuit. Hence, isolating the probe circuit from the measurement circuit ensured that no such interference would occur. A differential design was also implemented to ensure measurements weren't being taken relative to ground. The signal passed through a 1:1 scope probe prior to entering the TIA box. Within the box, the signal was read and amplified by an AMC3302 chip's evaluation board to produce a differential signal. This differential signal then passed through a 2x transimpedance amplifier similar in design to that of an ADC12, which could then be read by an oscilloscope. The output signal will then be between 0 and 5V, with the amplifier railing due to too little or too much signal, should it reach 0 or 5V, respectively. [19]

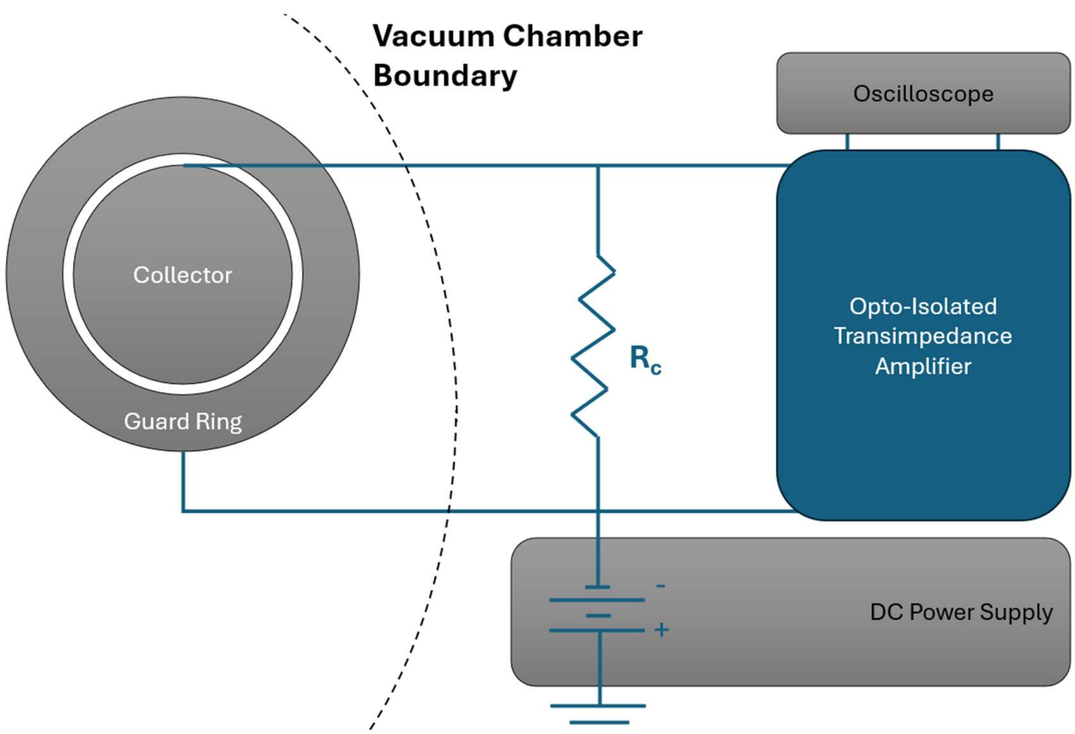

Figure 13: FP Circuit with Opto-Isolated TIA

Below, Figures Figure 14: FP Pulse Measurement Without Opto-Isolated TIA and Figure 15: FP Pulse Measurement with Opto-Isolated TIA illustrate the difference in the resolution of a pulse under the same test conditions, without and with the implementation of an opto-isolated TIA. Of note is the higher resolution of the rectangular pulse in space and time with the TIA compared to the more poorly resolved and diffuse signal collected without the TIA. A perturbation in the signal at approximately +20° is representative of a known facility effect within the chamber when taking Faraday probe measurements.

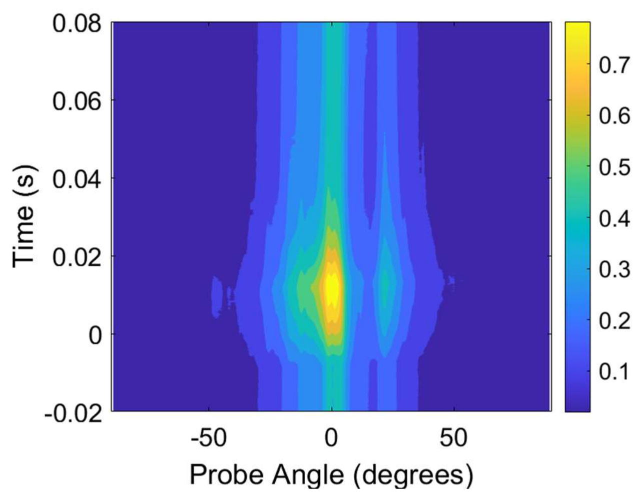

Figure 14: FP Pulse Measurement Without Opto-Isolated TIA

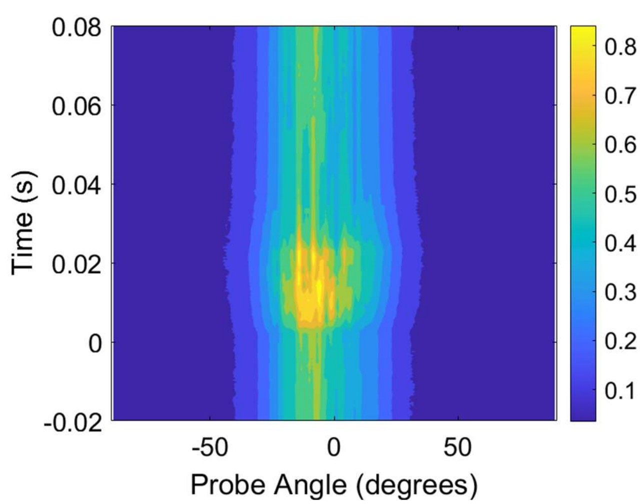

Figure 15: FP Pulse Measurement with Opto-Isolated TIA

Retarding Potential Analyzer Theory

A retarding potential analyzer (RPA) probe works, in principle, by using a series of grids biased to particular voltages to filter out the charges permitted to conduct to the collector plate and generate a current. In the RPA used for these experiments, four grids were used: a screening grid, a repeller grid, a discriminator grid, and a suppressor grid.

As particles from the thruster plume streamed toward the RPA, they first encountered the screening grid, an unbiased metallic grid electrically isolated from the rest of the probe. This screening grid served to minimize disturbances to the plasma caused by the repeller grid. After passing through the screening grid, the particles hit the repeller grid, biased to a high, positive fixed voltage, which serves to repel energetic ions not intended to be analyzed. Following this, the discriminator grid is specifically modulated to sweep a variety of positive voltages to only permit electrons satisfying particular criteria to make it through to the collector. The suppressor grid is used to attenuate the flow of any electrons generated through secondary electron emission at the collector plate. [20] The RPA used is illustrated below in Figure 16: RPA Wiring to Grids.

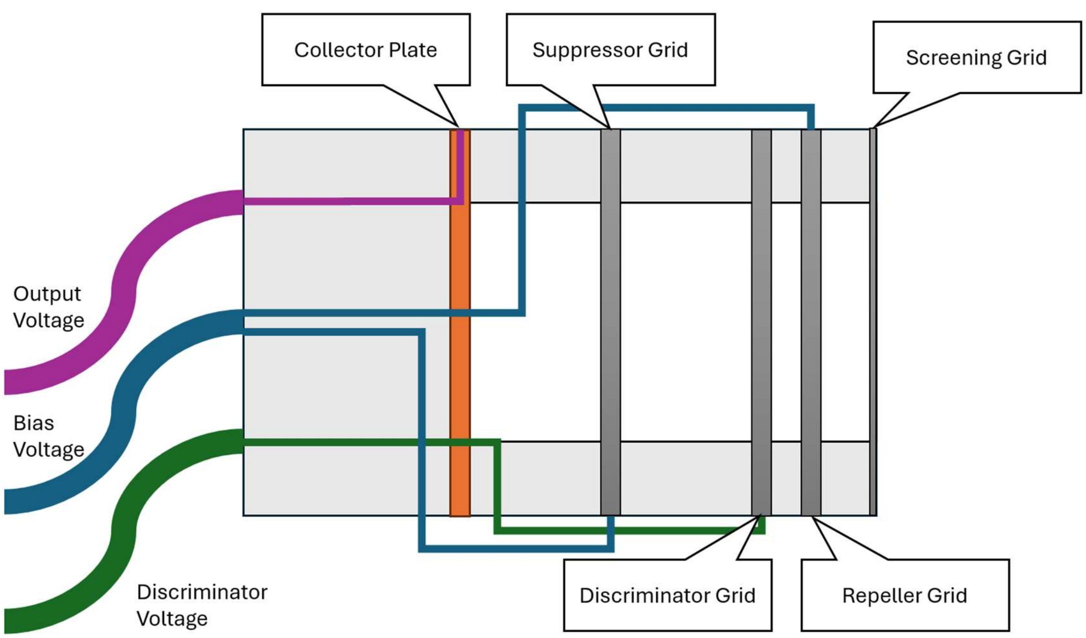

Figure 16: RPA Wiring to Grids

The RPA was mounted in the chamber onto an 80-20 aluminum extrusion stinger, set 20” downstream of the thruster and concentric to its exhaust channel, shown below in Figure 18: Installed RPA Relative to Thruster. The RPA’s swept discriminator voltage was supplied by a Kepco 500M bipolar operational power supply (BOP), while the fixed bias voltage was supplied by a TDK-Lambda GEN600-1.3 power supply. The current collected by the RPA was passed through an Oriel 70710 transimpedance amplifier (TIA) powered by two DC power supplies, one an OWON SPE6103 and the other a Kiprim DC310S, with its output signal displayed on a Siglent SDS2104X oscilloscope.

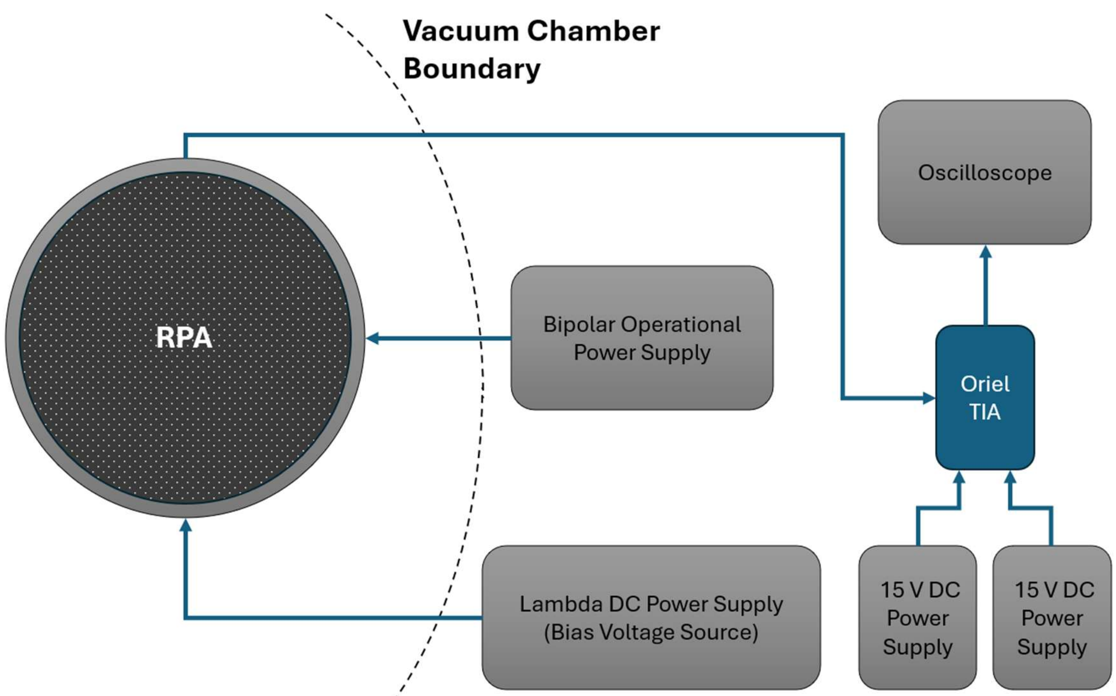

Figure 17: RPA Probe Integration

Figure 18: Installed RPA Relative to Thruster

The Oriel TIA was used to convert the current signal produced by the RPA to a voltage measurement that could easily be read on the oscilloscope. Practically speaking, because the current measured by the RPA was so weak, in order to facilitate the measurement of this signal, the TIA was used to convert this output current to a higher, measurable voltage with minimal noise. To operate, the TIA required two 15 V DC power supplies specified above, one biased negatively, the other, positively. The TIA was set to a gain of 10E6, with the oscilloscope sampling time and voltage intervals set to accommodate the RPA's output signal for each test case.

Probe Integration

Faraday and RPA measurements were taken separately, with the chamber reconfigured to accommodate operating one probe at a time during the suite of test points assessed during this campaign. This was done on account of the FP swept arm mechanically interfering with the positioning of the RPA and to mitigate any potential facility effects that could be created by operating either of the diagnostics in the presence of the other and perturbing the thruster plume.

The Faraday probe was mounted to a swept arm capable of rotating -90 to 90° relative to the center of the thruster plume. This swept arm was electrically isolated from the FP and amounted to a sweep distance of 21.25" from the face of the thruster. Power was routed to the FP through a vacuum feedthrough, with its output similarly being routed through another port on the same feedthrough flange. A 1072 Ω shunt resistor placed across the guard ring and collector BNC wires was used to measure the output signal from the FP.

The RPA was mounted to a linearly translating stage set to a distance of 20" from the face of the thruster, set to a height such that its collector grids were concentric to the thruster channel. Its bias and discriminator voltage connections were fed through the same feedthrough flange as the FP.

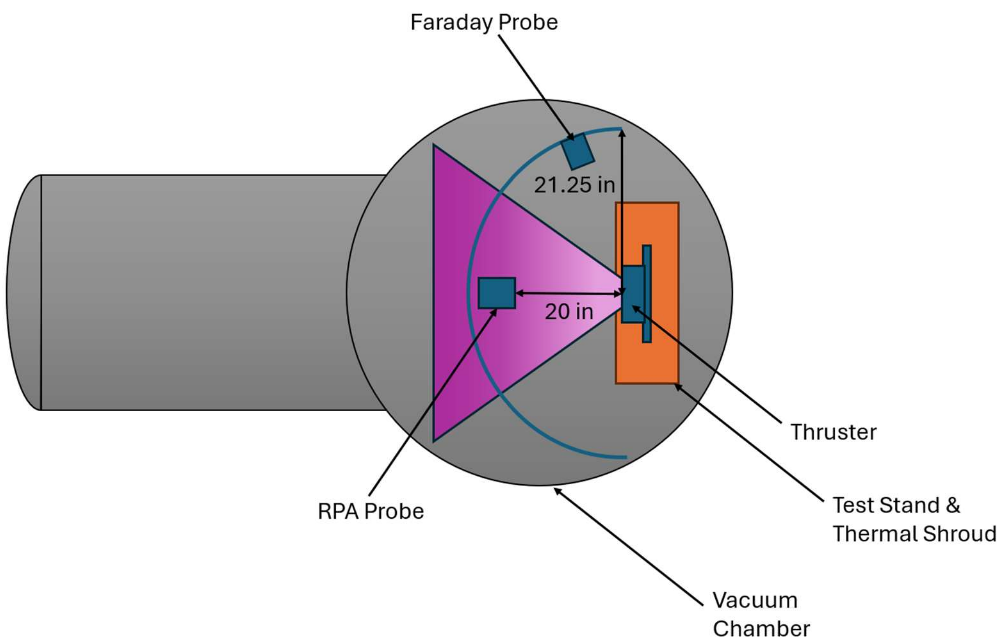

Figure 19: Diagnostic Systems Integration into Vacuum Chamber

The RPA was integrated into the vacuum chamber using a vertical, sting mount stand set 20 inches from the exhaust plane of the thruster. This position was set by a linearly actuating stepper motor translation stage. A 1 Ω shunt resistor was connected to the output leads of the probe on the vacuum chamber's outside interface.

Upon sustained operation of the RPA, it became apparent that performance was degrading, as output signals became increasingly low gain and noisy. The RPA was fully disassembled, where it was clear that graphite from the thruster's antenna was ablating off and depositing onto the grids and dielectric surfaces. The lowest resistance measured across these dielectric standoffs was only 11 Ω. After carefully removing a maximum amount of graphite using a combination of light abrasive and isopropyl alcohol and ensuring that the component resistance was acceptably high, on the order of MΩ, the RPA was reassembled and operated with no further issues.

Data acquisition

Data were primarily recorded on a Siglent SDS2104X oscilloscope for thrust, FP, and RPA measurements. This oscilloscope data was collected in time sample intervals of 1.0E-4 seconds and exported as .csv files for post-experimental processing. Temperature was monitored using temperature sensitive gradient tape applied to the thruster body and backplate.

Experimental summary

During a test campaign in Spring 2026, thrust and diagnostic measurements were taken for the thruster operating in both continuous and pulsed regimes using both krypton and ASCENT simulant as propellants. Only the data collected from krypton test points from this last campaign are presented and analyzed here. Figure 20: Integrated Thruster Operation, below, illustrates the thruster operating as the FP arm completes a sweep. It should be noted that the RPA (far left), was translated to its furthest possible axial position from the thruster during this FP sweep to minimize the potential for interference between the diagnostics and any impact on the plume.

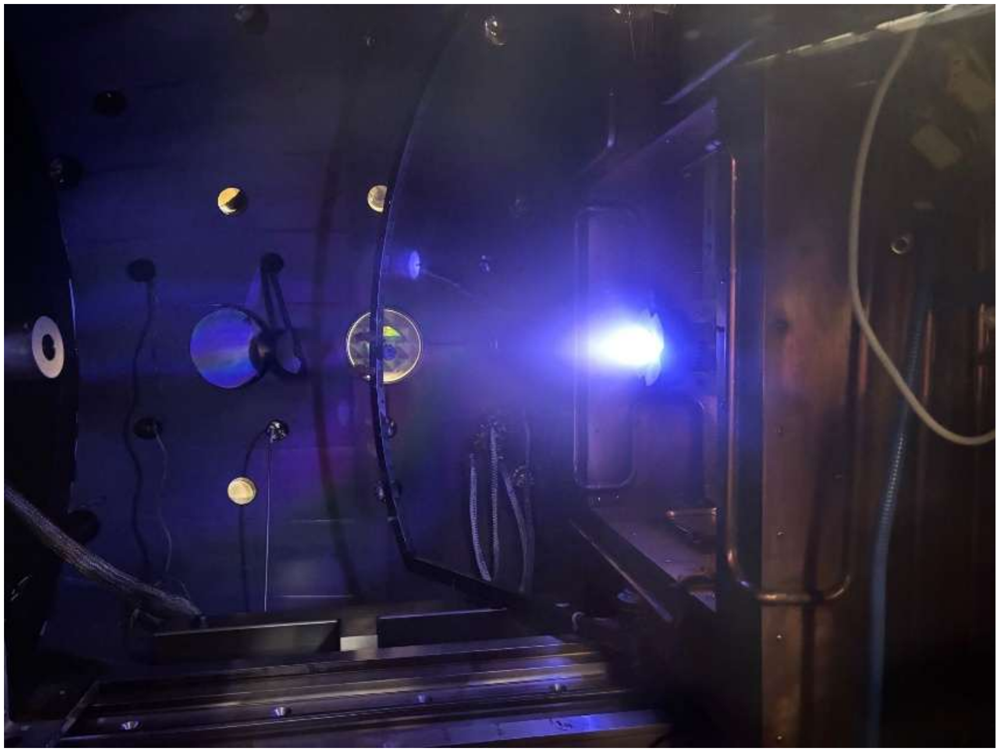

Figure 20: Integrated Thruster Operation

The primary purposes of this most recent test campaign were to evaluate any changes in thrust and specific impulse performance between continuous and pulsed operational regimes and characterize the properties of the plume generated during pulsed operation using diagnostic tools. Prior campaigns had focused on characterizing a broad spectrum of test conditions, sweeping mass flow rate, input power, pulse properties, and using a variety of propellants.

Using the results obtained from these past campaigns, operating conditions for this campaign were selected based on what had yielded the best thrust performance previously, with more targeted ranges of settings used as independent variables of interest to manipulate throughout new tests. These test conditions are detailed below in Figures Figure 21: Steady State Test Condition Summary and Figure 22: Pulsed Test Condition Summary . For pulsed test points, duty cycle was progressively increased from 0.2 to 1 in increments of 0.2, minimum pulse power was held steady at 30 W, and maximum pulse power was progressively increased throughout the test points selected to assess performance over a series of average powers comparable to those the thruster operated with in steady state. To characterize the plasma physics of the plume generated under a pulsed operating regime, two pulsed conditions, P6 and P8, as detailed in Figure 22: Pulsed Test Condition Summary below, that had been identified as being of interest in terms of high performance, were selected to be the conditions under which both Faraday probe and RPA measurements were taken.

All krypton tests were operated with a 3 sccm flow rate (1.87E-01 mg/s). The average vacuum pressure held throughout all test points was 9.70E-06 Torr with a standard deviation of 5.30E-06 Torr, and pressure was continuously monitored throughout testing using an ion gauge.

Figure 21: Steady State Test Condition Summary

Test Condition	Power Setting (W)
S1	10
S2	20
S3	30
S4	40
S5	50
S6	75
S7	100
S8	125
S9	150
S10	200
S11	250
S12	300
S13	350
S14	400

Figure 22: Pulsed Test Condition Summary

Test Condition	Maximum Power (W)	Minimum Power (W)	Pulse Length (s)	Pulse Period (s)	Duty Cycle	Nominal Average Power (W)
P6	100	30	0.02	0.1	0.2	44
P7	100	30	0.04	0.1	0.4	58
P8	100	30	0.06	0.1	0.6	72
P9	100	30	0.08	0.1	0.8	86
P10	100	30	1	0.1	1	100
P16	200	30	0.02	0.1	0.2	64
P17	200	30	0.04	0.1	0.4	98
P18	200	30	0.06	0.1	0.6	132
P19	200	30	0.08	0.1	0.8	166
P20	200	30	1	0.1	1	200
P26	300	30	0.02	0.1	0.2	84
P27	300	30	0.04	0.1	0.4	138
P28	300	30	0.06	0.1	0.6	192
P29	300	30	0.08	0.1	0.8	246

Performance analysis

From all experimental data, as collected, we can make several comparisons of this thruster's performance compared to that published by other research groups. Several metrics stand out in terms of importance for assessing the performance of this thruster: specific impulse, total thruster efficiency, thrust-to-power ratio, mass utilization efficiency, and average divergence. [21] The total thruster efficiency is defined as the ratio of thrust generated to the maximum possible thrust generated if all power supplied were converted into a perfectly collimated beam of kinetic energy expelling out of the thruster:

$$\eta_T = \frac{T^2}{2\dot{m}P_e},$$

where T is the measured thrust produced, $\dot{m}$ is the propellant mass flow rate, and P_e is the power supplied to the thruster. The thrust-to-power ratio is simply defined as the ratio of the measured thrust to power supplied for a constant total thruster efficiency, and is inversely proportional to specific impulse. The mass utilization efficiency represents the ratio of ionized propellant flow to total propellant flow, and is given by the following equation:

$$\eta_m = \frac{\frac{M}{e} J_{tot}}{\dot{m}},$$

where J_{tot} is the total ion current and e is the electron fundamental charge. [21] Divergence was characterized using both the full width half maximum (FWHM) and the average divergence. The FWHM is calculated by fitting a Gaussian function to the current data, then retrieving its associated standard deviation and multiplying by a factor of 2.355. The average divergence is calculated using the following equation:

$$< \cos(\theta) >_{mv} \approx \frac{2\pi R^2 \int_0^{\frac{\pi}{2}} J[\theta] \cos(\theta) \sin(\theta)\, d\theta}{2\pi R^2 \int_0^{\frac{\pi}{2}} J[\theta] \sin(\theta)\, d\theta} \approx < \cos(\theta) >_J,$$

where each integral was evaluated over the arc of the Faraday probe's sweep. [22]

The maximum mass utilization efficiency was calculated from Faraday probe data, where the ionized species flow rate was obtained by integrating the measured current over the surface of the probe. This value was plotted over the duration of a single thruster pulse. All campaigns thus far have only focused on collecting diagnostic data for the P6 and P8 conditions, as these were of primary interest to the project. Only data collected during this most recent campaign is presented.

Two MATLAB scripts were used to read in and process raw .csv files from both the RPA and FP. For the RPA, the regions of interest, highlighted below in yellow, were isolated by selecting start and end indices corresponding to them. Either the left or right side of the current trace could be used, so long as it was ensured that no bias voltage sweep values would be repeated, resulting in different current measurements for the same input voltage.

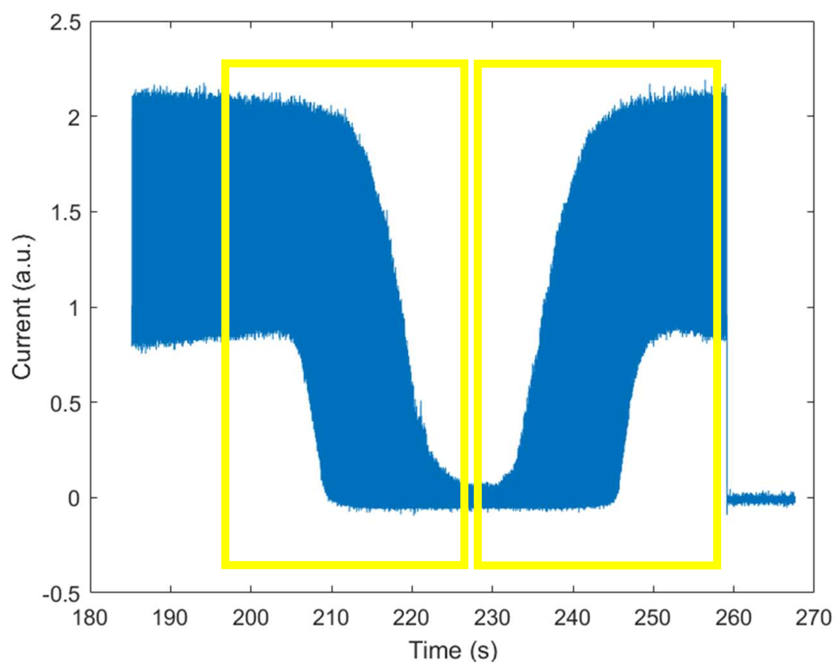

Figure 23: Sample Unprocessed RPA Trace

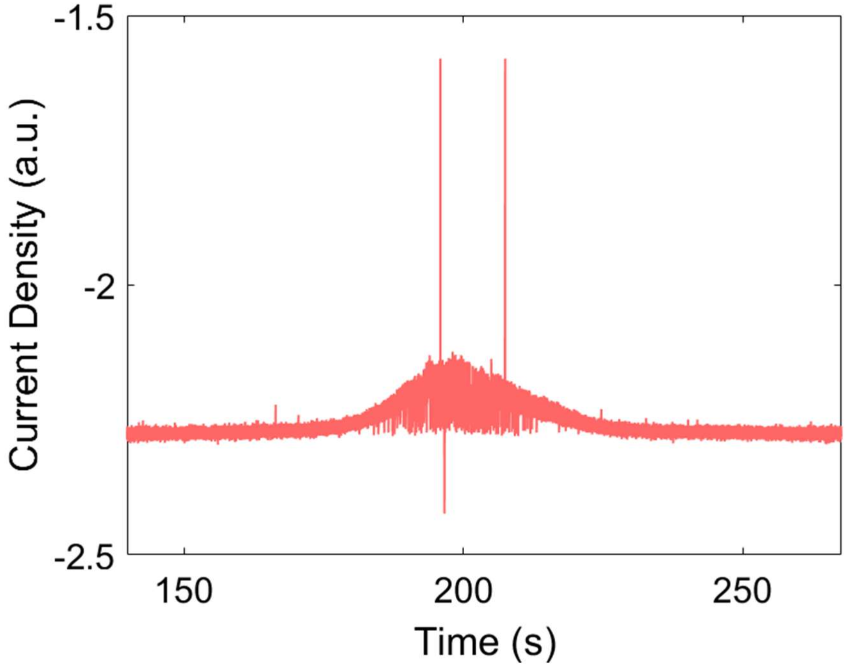

Figure 24: Sample Unprocessed FP Trace

The RPA and FP scripts were adapted from an existing set of Mathematica scripts and expanded to meet the scope of the analyses requested for this project. Improvements were also made in terms of contour mapping computational efficiency and the method by which raw data were initially averaged and smoothed prior to analysis. This resulted in significantly faster data processing, on the order of seconds, compared to the prior scripts, which took minutes to run. A third script was used to generate thrust and specific impulse plots with respect to power delivered to the thruster. The results generated from these scripts are presented below in the tables below.

To calculate the mass utilization efficiency, the current collected during a pulse was integrated over the surface of the FP to calculate an ion flux, which was then compared to the total propellant mass flux at the FP's distance from the thruster.

Results

Thrust results

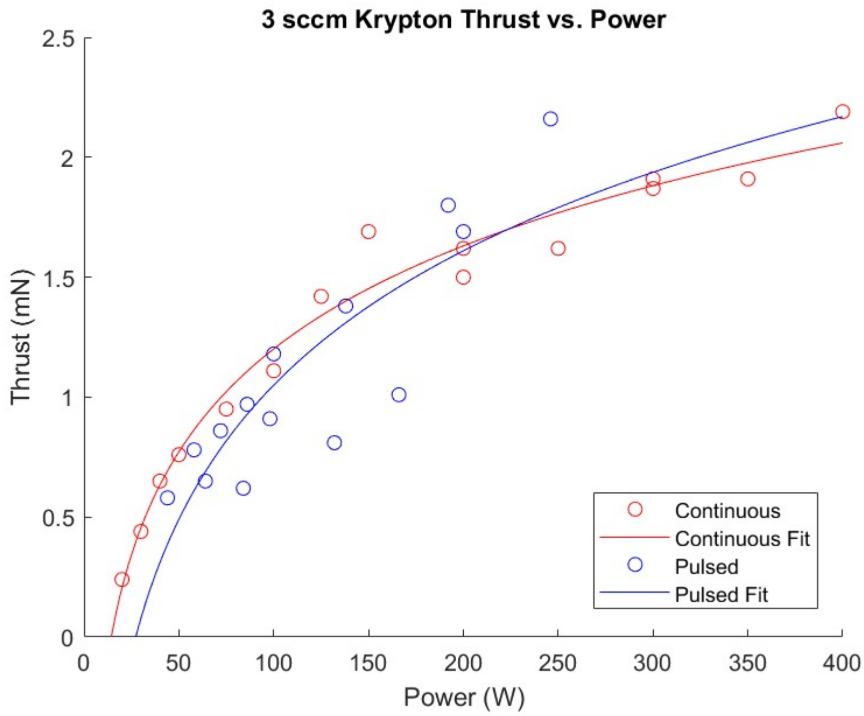

Figure 25: Thrust Stand Measurement Results

No significant overall separation of trends appeared to be observed in terms of thrust for operating in a pulsed vs continuous regime given the data collected. Any improvements in performance from operating on a pulsed regime were expected to be in terms of improvements in power efficiency rather than increasing thrust. However, given how comparable the pulsed vs continuous performances were, this is potentially a good indication that any benefits associated with pulsed operation are not accompanied with significant degradation in thrust performance. These results come with a strong disclaimer that due to the limited number of tests completed, some amount of error is expected. Ideally, further testing would entail several repeated measurements for each test point and extended characterization of sources of compounding error throughout the collection and analysis of this test data.

During the data collection for one of the two pulsed points lying noticeably below the trendlines, it should be noted that the floating potential measured throughout testing was not stable, and that transient phenomena appeared to be impacting the thruster's performance negatively, even with repeated attempts to take a clean measurement. The thruster appeared to be switching between two operating modes, particularly for the P19 case (166 W delivered). This behavior was observed for P18, P19, and P20, with the P20 case not remaining lit beyond several seconds of operation.

I_{sp} results

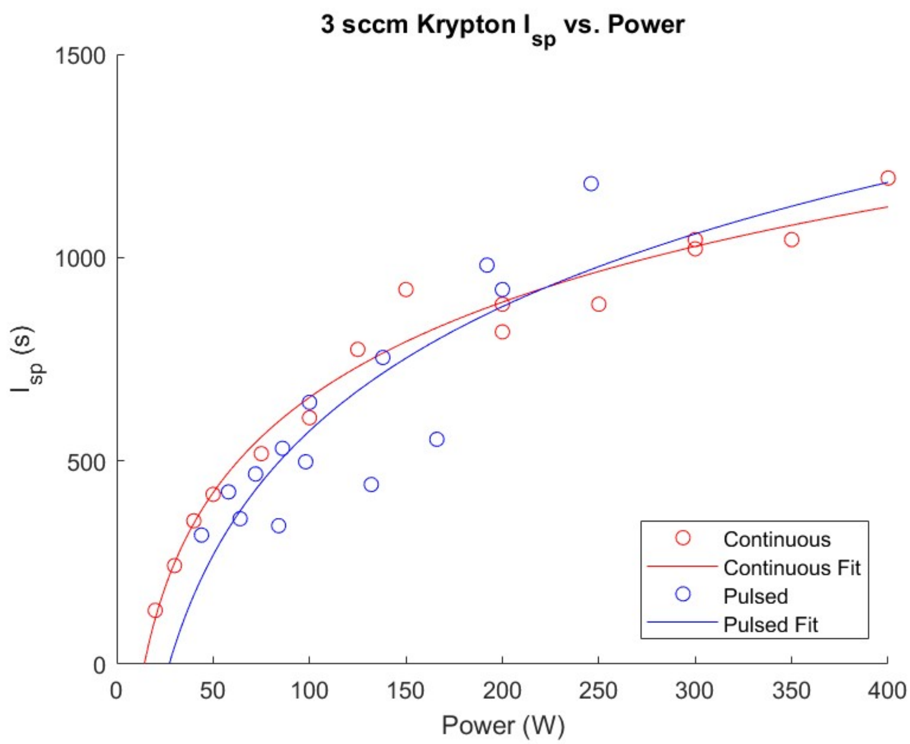

Figure 26: Thrust Stand-derived Specific Impulse

Similarly to the thrust case, the I_{sp} did not appear to show significant decreases in performance relative to the continuous case at low powers. Again, due to the limited number of tests completed, these results would require further testing with repeated test points and detailed error analysis to draw any definitive conclusions beyond what's apparent from this data alone. At higher powers in excess of 160 W, the pulsed tests appeared to yield increases in specific impulse relative to continuous operation.

In terms of comparable published data, Sheppard found that for steady state operation on krypton at 0.19 mg/s (~3 sccm) and 190 W of input power, specific impulse approached ~600s. A comparable test point from this campaign, 192 W under pulsed operation, yielded a specific impulse of ~981 s, a greater than 60% increase in performance for the same operating conditions. [5] Under steady state conditions, with a comparable input power of 200 W, yielded a specific impulse averaging at 851 s. Relative to both Sheppard's data and the continuous data collected in this campaign, the pulsed testing yielded consistently higher specific impulses at higher average powers.

RPA results

From the raw RPA data files generated throughout the experiments, the collected data were initially smoothed using a moving average scheme. Following this, the data were sliced relative to the pulse parameters set for the particular test point being evaluated using a monotonic interpolating slice function: MATLAB's native Piecewise Cubic Hermite Interpolating Polynomial (PCHIP) interpolation scheme. A starting index needed to be selected such that it corresponded with the start time of a pulse. This function generated time slices for collector current and bias voltage for a particular time queried. At three time slices, one at the start of a pulse (red), one at the end (green), and one 0.02 s following (blue), collector current was plotted against bias voltage in Figures Figure 27: Krypton P6 Collector Current vs. Bias Voltage and 30 below.

To generate the contour plots shown below in Figures Figure 29: Krypton P6 Current Density Contour Plot and Figure 32: Krypton P8 RPA Current Density Contour Plot, 3-dimensional arrays were defined for the ion energy distribution function (IEDF). These arrays were populated by voltage on the first layer and time on the second, repeating in every column. For the third layer, a spline interpolation was applied to the time gradient of the current data collected at a particular time slice, yielding the IEDF. Following this, the average beam voltage was calculated by taking the integral of the voltage multiplied by the IEDF from the minimum to maximum bias voltage and dividing by the integral of the IEDF alone over the minimum to maximum bias voltage, with both integrals taken with respect to voltage. The contour plots were generated by applying a squeeze function to each layer of the array and using MATLAB's native contourf function.

KrP6 RPA Results

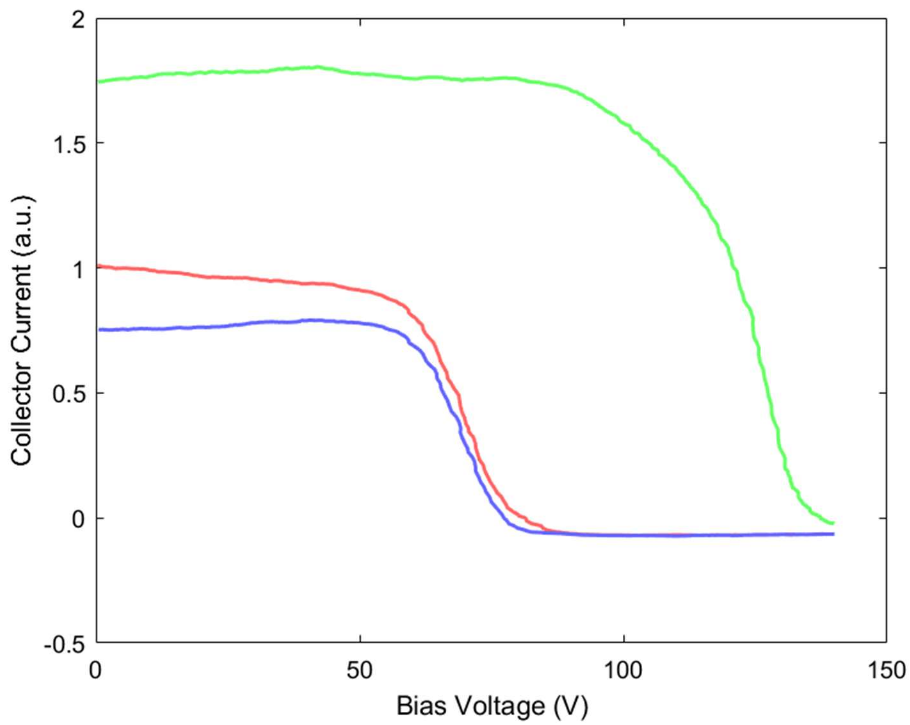

Figure 27: Krypton P6 Collector Current vs. Bias Voltage

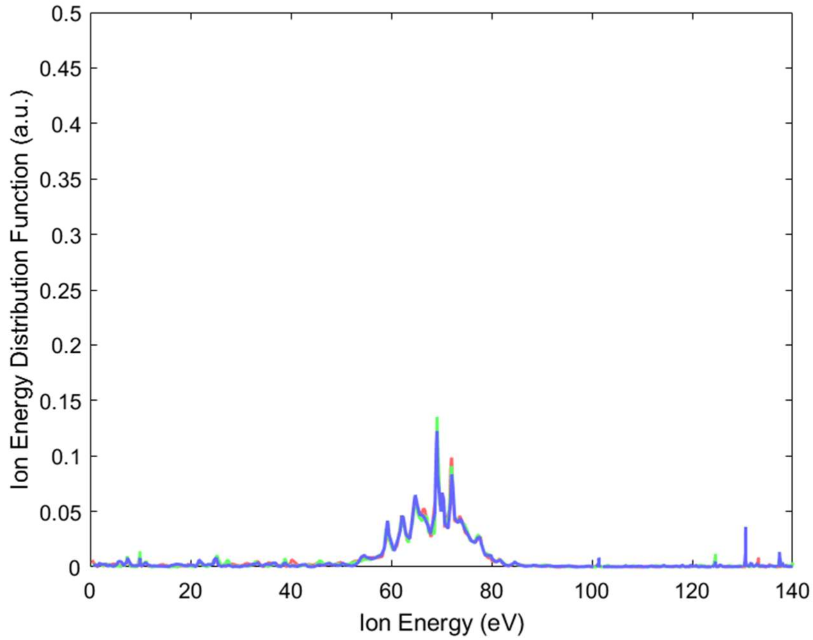

Figure 28: Krypton P6 IEDF vs. Ion Energy

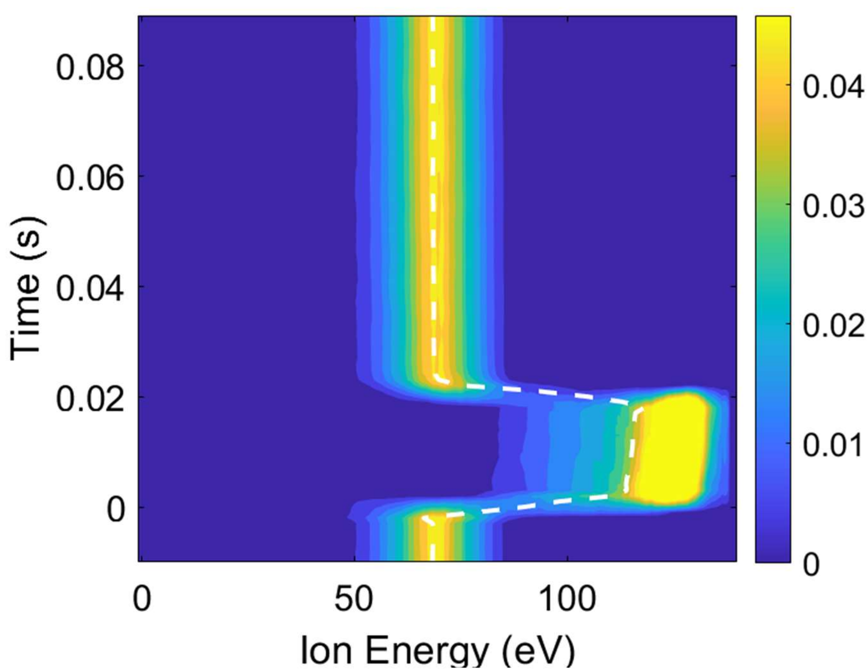

Figure 29: Krypton P6 Current Density Contour Plot

KrP8 RPA Results

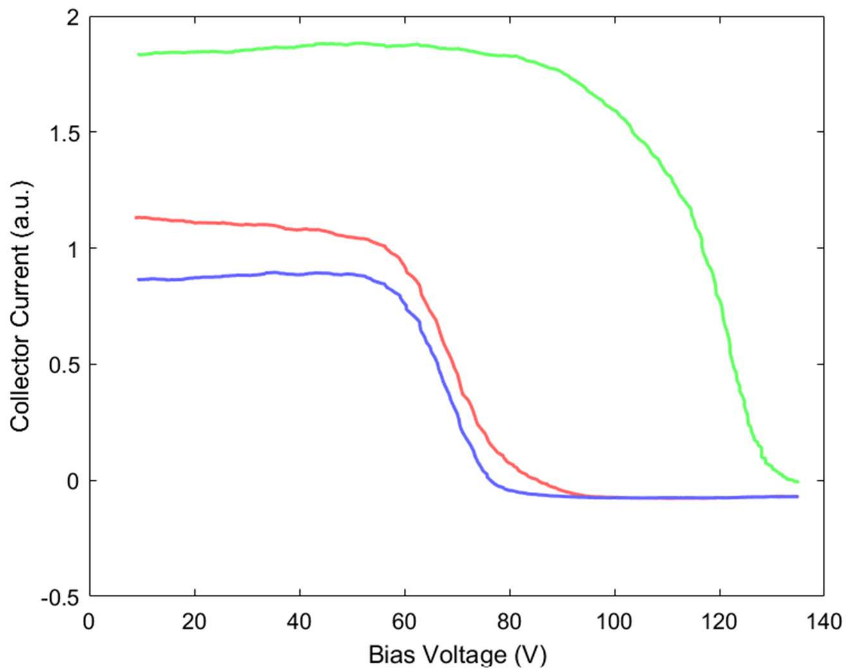

Figure 30: Krypton P8 Collector Current vs. Bias Voltage

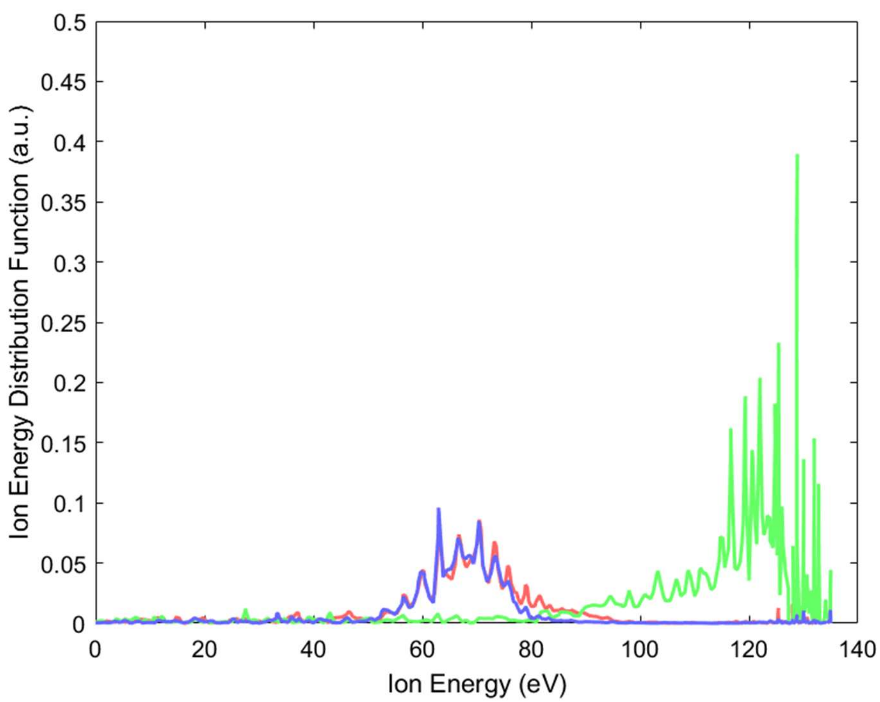

Figure 31: Krypton P8 IEDF vs. Ion Energy

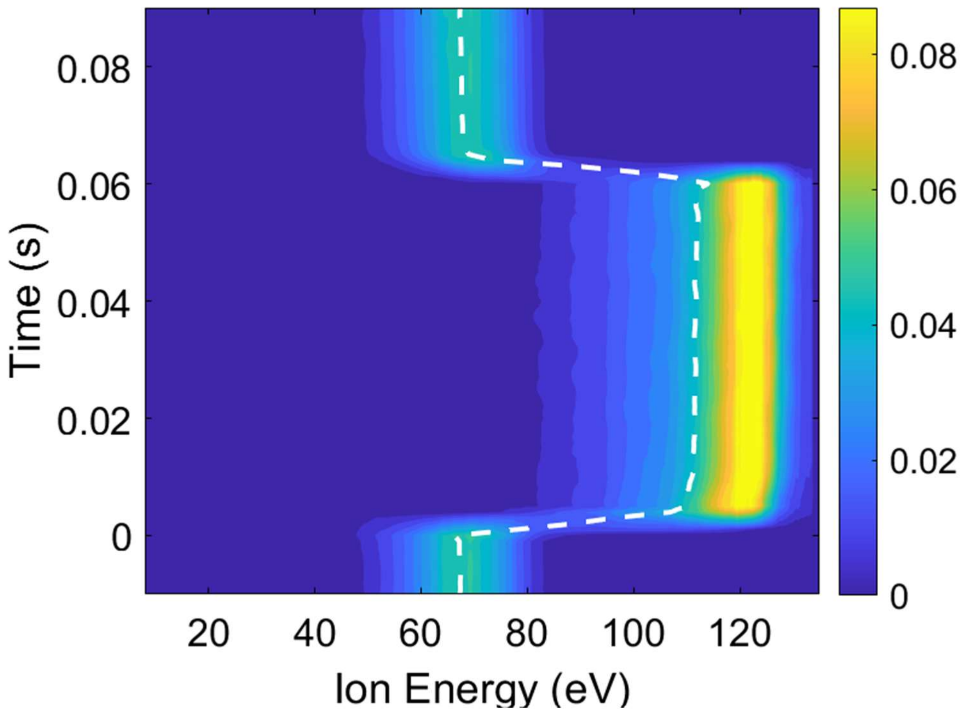

Figure 32: Krypton P8 RPA Current Density Contour Plot

In the figures above, the green lines represent the current measured at the end of the pulse for both cases. This end collector current is marginally higher in the P8 condition relative to the P6 condition. This is potentially explained by the fact that an operating regime in which the extended pulse duration of P8 would provide additional time to drive further ionization within the thruster's plume. This increased ionization could be caused by the growth of a larger free electron population capable of driving further collisions within the plume. The currents associated with the red line, in particular, are the most uncertain, as the properties associated with these time slices are very sensitive to pulse start time selection, and some amount of error is expected if the power ramp start time is not selected precisely enough, leading to part of the ramp being erroneously captured instead. The red line represents current at the initiation of the pulse, while the blue line represents current 0.02 s after the termination of the pulse.

In the two contour plots above, the dashed line represents average beam voltage over the pulse. Very minimal change was observed in terms of average beam voltage between the P6 and P8 test conditions, so this beam voltage appear characteristic of the maximum and minimum power settings selected rather than dependent on any transient behavior associated with changes in duty cycle. However, comparing between these two conditions, the current density is considerably higher for the P8 condition compared to the P6 condition. Under the P6 condition, the current density is notably more uniform at both the maximum and minimum power portions of the pulse, with most ion energies clustered around 60-80 eV. In the P8 case, the current density is approximately twice as high at the pulse maximum compared to the P6 case, while the pulse minimum remains comparable to that of the P6 case.

Within the time slice plots of IEDF illustrated in Figures Figure 28: Krypton P6 IEDF vs. Ion Energy and Figure 31: Krypton P8 IEDF vs. Ion Energy above, a more interesting picture begins to emerge in terms of the distribution of the ions' energies than can be observed in the contour plots alone. On first glance, the contour plots appear to show that P8 is simply a stretched-out version of P6 in time. However, in comparison, for the P6 condition, the time slice plot appears to illustrate a lower energy and more uniform distribution of energies over time, whereas for the P8 condition, there is a high concentration of high energy ions in the middle of the pulse in excess of 100 eV, with a similar distribution of low energy populations from 60-80 eV.

Both P6 and P8 appear to generate a relatively small amount of low energy, ionized populations below 60 eV. The largest populations all exceed the 14 eV threshold for single krypton ionization, showing that both conditions yield a high degree of ionization within the exhaust. [23]

FP results

Similarly to the RPA script, the FP script takes the raw FP current trace, applies a DC offset and moving average for smoothing, and then uses the same slice function to calculate current density at specifically queried time slices, with the same time slice color convention as established for the RPA. In addition to the data collected, the script uses the physical properties of the probe and krypton propellant supplied as well as the pulse parameters set for a particular test point. To generate current density contour plots, time, probe angle, and current are built up in a 3-dimensional array, using the same methods as with the RPA. All remaining quantities of interest obtained with the FP data, including FWHM, mass utilization efficiency, and plume divergence are calculated using the methods described in the Performance Analysis section preceding these results.

For the mass utilization efficiency, specifically, the slice function was integrated with respect to sweep angle, and this integral quantity was used in the equation below to calculate this efficiency:

$$\eta_m = \frac{m_i \pi L_p^2}{\dot{m}e} * \frac{\pi}{180}\left(-\int_{-4}^{0} (SliceFunction(\theta) * \theta)d\theta + \int_{0}^{90} (SliceFunction(\theta) * \theta)d\theta\right),$$

where m_i is the ion mass of krypton, L_p is the distance from the thruster to the Faraday probe, $\dot{m}$ is the propellant mass flow rate, e is the electron fundamental charge, and θ is the probe angle in degrees.

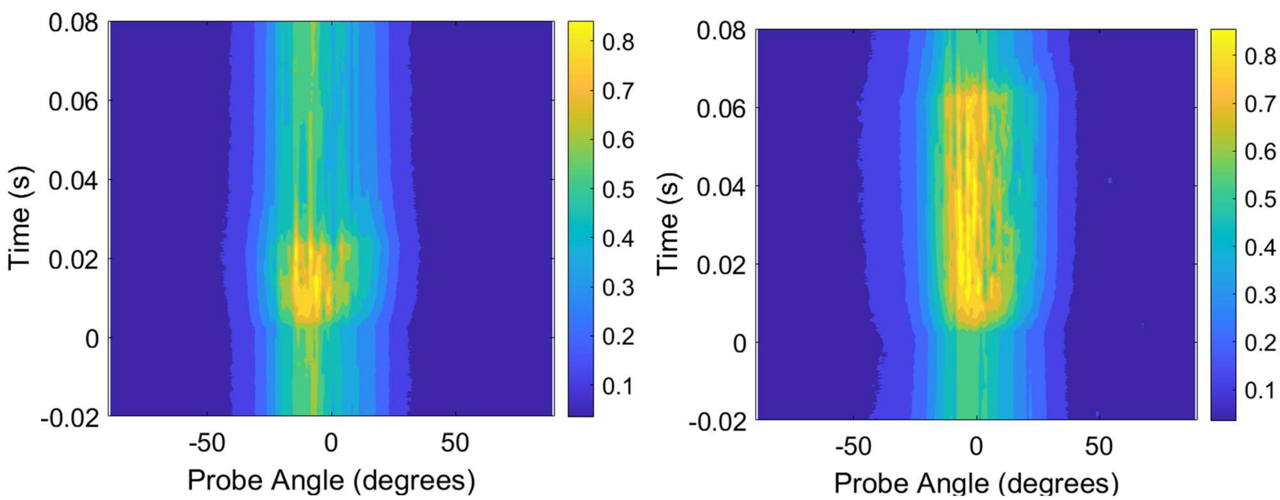

Figure 33: FP Current Contour Plots : a) Krypton P6, b) Krypton P8

Similarly to the RPA results, as illustrated in Figures Figure 34: Krypton P6, a) Current Density vs. Probe Angle, b) Mass Utilization vs. Time, c) FWHM vs. Time, d) Average Plume Divergence vs. Time and Figure 35: Krypton P8, a) Current Density vs. Probe Angle, b) Mass Utilization vs. Time, c) FWHM vs. Time, d) Average Plume Divergence vs. Time a), the current density is higher for the P8 condition than the P6 condition, though not as dramatically, with what amounts to a 30% difference between the two. In

Figure 33: FP Current Contour Plots : a) Krypton P6, b) Krypton P8 above, the two contour plots show similar uniformity in current density for the two test conditions. The vertical striations in the high current density regions appear to be artifacts of potential mismatching between the position logging of the swept arc and the point of time in the pulse at which the probe measurement is taken. At approximately 5°, there is a noticeable decrease in measured current density that can be seen in both

Figure 33: FP Current Contour Plots : a) Krypton P6, b) Krypton P8 above and in Figures and Figure 35: Krypton P8, a) Current Density vs. Probe Angle, b) Mass Utilization vs. Time, c) FWHM vs. Time, d) Average Plume Divergence vs. Time below. This is a known facility effect associated with testing in STF.

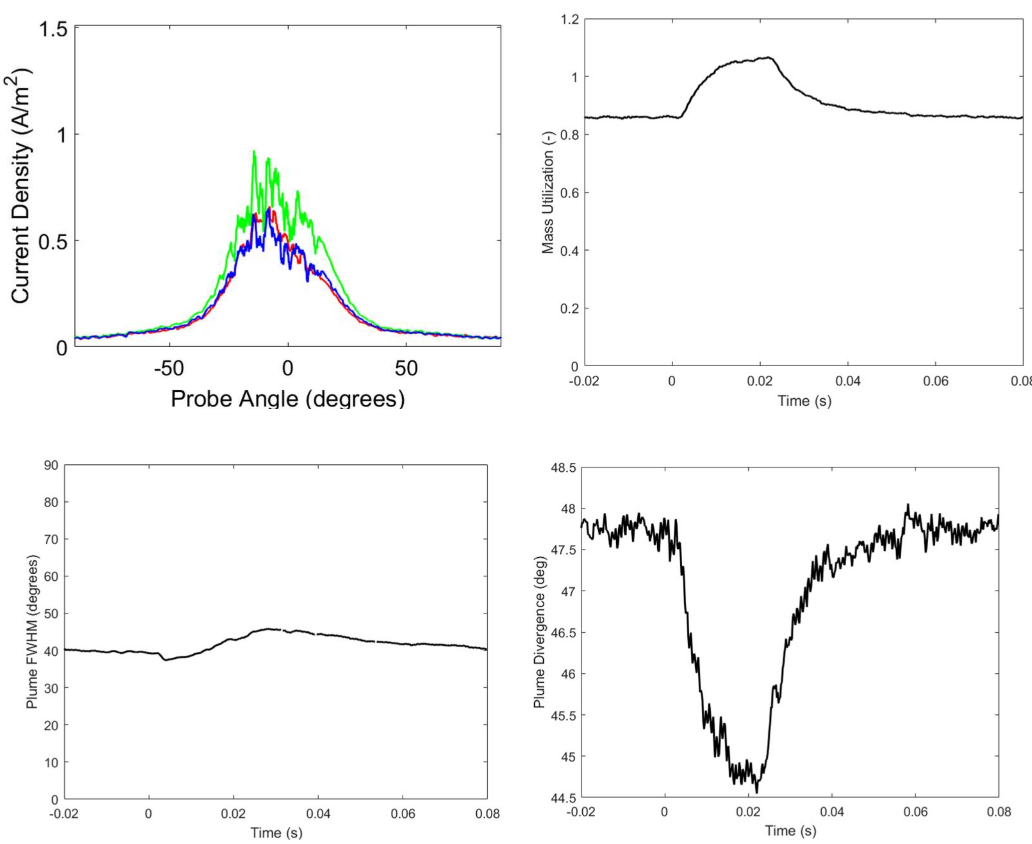

Figure 34: Krypton P6, a) Current Density vs. Probe Angle, b) Mass Utilization vs. Time, c) FWHM vs. Time, d) Average Plume Divergence vs. Time

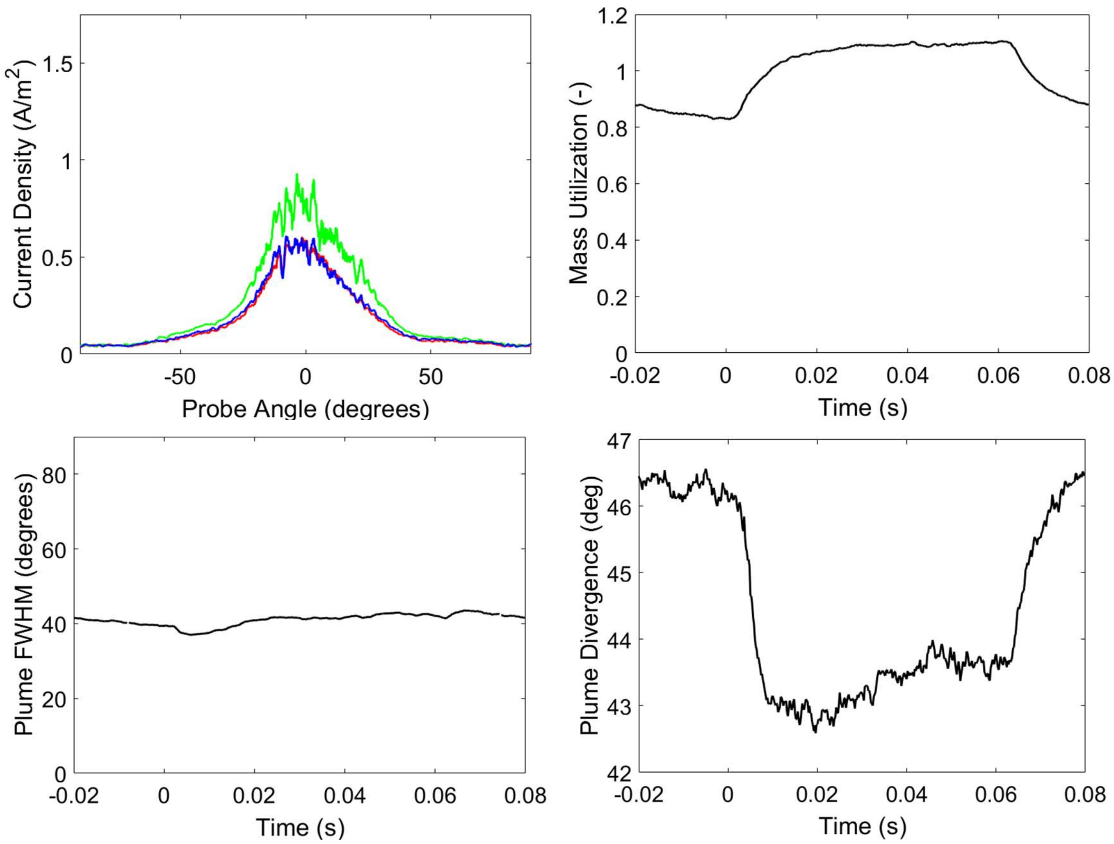

Figure 35: Krypton P8, a) Current Density vs. Probe Angle, b) Mass Utilization vs. Time, c) FWHM vs. Time, d) Average Plume Divergence vs. Time

Comparing the results from P6 to P8, it can be seen that the plume divergence is higher for P6 than P8, and that P8's divergence remains more stable throughout the pulse. The P8 condition has a more marked transition between the on and off conditions, quickly damping any transient increases and decreases at the start and end of the pulse. The FWHM plots are less dramatic, but illustrate a similar trend between the P6 and P8 cases. In both, the FWHM first decreases prior to rising steadily at the end of the pulse before yet again decreasing to return to its initial value. For P8, this trend is flatter than in the P6 case, indicating more consistent behavior throughout the pulse. Similarly to the RPA measurements taken, the current density at the end of the pulse is higher in the P8 case than the P6 case. For the P6 case, the current density fluctuation is significantly noisier, with less differentiation at different time slices throughout the pulse.

In terms of mass utilization efficiency, more anomalous behavior is observed for both test cases. As mass utilization efficiency is defined in terms of the ratio of ionized propellant mass flux to total propellant mass flux, it is not physically possible for this quantity to exceed 1. An issue noted in prior test campaigns at the University of Michigan's PEPL was that within the plume generated by the thruster, the FP's sheath region was larger than expected, generating a larger effective collection area and artificially increasing the ion flux measured. This facility effect was also documented in *Electrical Facility Effects on Faraday Probe Measurements* by Frieman et al. [24] This similarly appeared to be the case in this campaign, as the maximum mass utilization over a single pulse was in excess of 1 for both the P6 and P8 conditions. This larger effective probe area meant that a greater amount of ion flux was collected than accounted for using the probe's physical geometry alone, as was done in the FP data analysis script.

From Figures Figure 34: Krypton P6, a) Current Density vs. Probe Angle, b) Mass Utilization vs. Time, c) FWHM vs. Time, d) Average Plume Divergence vs. Time and Figure 35: Krypton P8, a) Current Density vs. Probe Angle, b) Mass Utilization vs. Time, c) FWHM vs. Time, d) Average Plume Divergence vs. Time c) alone, comparisons can still be drawn in terms of overall trends observed for the two test conditions. Both cases feature nearly identical transient behavior, with what appears to be an exponential rise and decay at pulse initiation and termination on approximately the same timescale. Both pulse initiation and termination appear to take 0.02 s to manifest their full effects on the mass utilization. These characteristics of the pulse profile seem to occur independently of the power setting used, as neither the speed of the initiation and termination nor the magnitude of the change in mass utilization efficiency appear to change significantly.

In the P6 case, mass utilization never reaches steady state, beginning to decay almost just as soon as it reaches its peak value, since its high-power pulse duration is only 0.02 s. In the P8 case, the mass utilization trends slightly upwards throughout the pulse, but appears to otherwise illustrate consistent behavior. P6 peaks at a mass utilization efficiency of ~1.05, while P8 peaks at ~1.1. In contrast to this, during the low power portions of a pulse, P6 holds steady at ~0.87, while P8 appears to not reach a steady state due to its shorter low power duration, varying between ~0.82-0.88. Overall, P8 appears to correlate with marginally higher mass utilization efficiency, though not dramatically so.

It should also be noted that the P20 case appears to be an outlier. This was likely caused by the inverted pendulum thrust stand contacting the thermal shroud and sticking, generating an erroneously large deflection measurement for the provided impulse from the thruster.

Summary of Results

Figure 36: Steady State Performance

Test Condition	Average Power Delivered (W)	Thrust (mN)	Efficiency (%)	Specific Impulse (s)	Thrust-to-Power (mN/W)
S1	0	0	0	0	0
S2	20.70	0.24	0.76	132	0.0117
S3	32.20	0.44	1.64	242	0.0138
S4	43.30	0.65	2.58	353	0.0149
S5	54.30	0.76	2.89	418	0.0141
S6	85.30	0.95	2.82	518	0.0111
S7	111.20	1.11	2.97	606	0.0100
S8	143.80	1.42	3.74	774	0.0099
S9	168.20	1.69	4.53	921	0.0078
S10	207.00	1.56 (avg)	3.15	851	0.0068
S11	252.25	1.62	2.79	885	0.0064
S12	299.70	1.89 (avg)	3.22	1037	0.0063
S13	344.50	1.91	2.84	1044	0.0056
S14	389.70	2.19	3.29	1195	0.0056

Figure 37: Pulsed Performance

Test Condition	Average Power Delivered (W)	Thrust (mN)	Efficiency (%)	Specific Impulse (s)	Thrust-To-Power (mN/W)	Max Mass Utilization Efficiency	Minimum Average Divergence (deg)
P6	44	0.58	2.04	317	0.0131	1.07	44.5
P7	58	0.78	2.70	424	0.0130	1.11	42.6
P8	72	0.86	2.63	468	0.0114	[redacted]	[redacted]
P9	86	0.97	2.82	531	0.0108	[redacted]	[redacted]
P10	100	1.18	3.37	644	0.0107	[redacted]	[redacted]
P16	64	0.65	1.74	358	0.0099	[redacted]	[redacted]
P17	98	0.91	2.16	498	0.0088	[redacted]	[redacted]
P18	132	0.81	1.27	442	0.0059	[redacted]	[redacted]
P19	166	1.01	1.62	553	0.0060	[redacted]	[redacted]
P20	200	1.69	3.54	921	0.0078	[redacted]	[redacted]
P26	84	0.62	1.59	340	0.0095	[redacted]	[redacted]
P27	138	1.38	4.24	754	0.0115	[redacted]	[redacted]
P28	192	1.80	4.91	981	0.0102	[redacted]	[redacted]
P29	246	2.16	5.53	1182	0.0095	[redacted]	[redacted]

The maximum specific impulse obtained for krypton propellant during this campaign was with the P29 test condition, yielding 1182 s. Under this test condition, the pulse length was 0.08 s over a 0.1 s cycle, reaching a maximum power of 300 W, with a minimum power of 30 W. At this same condition, thrust efficiency reached 5.53%.

Prior ECR test campaigns in the SPACE Lab conducted by Sheppard on PEPL's APEX thruster resulted in a thrust of ~1 mN for delivered power of approximately 175 W for a similar mass flow rate of 0.190E-06 kg/s of krypton. [5] Compared to this, the thruster evaluated in this campaign generated a thrust of 1.8 mN for a delivered power of 192 W under pulsed operation. Scaling to match the difference in power delivered between these points still results in a ~60% improvement on thrust for this current design over the prior APEX design.

Conclusions

This campaign assessed the performance of an electron cyclotron resonance thruster operating at 2.45 GHz under both a steady state and pulsed operating regime. Thrust measurements were taken using an inverted pendulum thrust stand, while Faraday probe and RPA measurements were taken to characterize the thruster's plume. Results for krypton propellant testing were presented here. Data from thrust stand measurements were analyzed to characterize the impact of repetitively pulsing the thruster on any associated degradation in thrust, and results were also presented in terms of specific impulse to provide more straightforward points of comparison to other published data. Data from the Faraday probe and RPA were used to assess the plume properties of the thruster and associated differences in plume ion species' distribution under different average operating powers and duty cycles. Results obtained from analysis of both thrust and diagnostic data were compared to prior ECR thruster performance characterization completed within the SPACE Lab.

Compared to steady state operation, pulsed operation appeared to show comparable thrust measurements for the same average power delivered. For the two pulsed operation conditions evaluated, the longer high power pulse duration case, P8, yielded marginally higher mass utilization efficiency and current density, with smaller plume divergence angle and FWHM, as derived from Faraday probe data. Further testing and characterization would be preferred to draw more definitive conclusions in comparing between steady state and pulsed operation.

In addition, after analyzing the RPA probe data, it was observed that the P8 case yielded a significantly larger population of ionized species exceeding energies of 100 eV during the high-power portion of the pulse, while the P6 case showed a nearly identical ion energy distribution throughout all times in a pulse between 60-80 eV with no comparably large high energy population. This appears to indicate that operating on a longer duty cycle pulse regime appears to correlate with reaching a threshold at which highly energetic species are able to form and persist during the pulse before returning to their baseline state as established in the P6 case.

From these results, it appears that it is possible to maintain much of the same performance obtained with a continuously operating thruster under a repetitively pulsed regime, though this requires further characterization to make any definitive argument. The exact optimization between the complexity of implementing a high-power switching system capable of sustaining such a regime and any savings in terms of spacecraft power required for a pulsed vs continuous thruster's operation is highly sensitive to a particular spacecraft's architecture and mission profile. High power switching systems can be challenging to implement in full-scale spacecraft due to their mass and overall size, but developments in solid state switch miniaturization and power handling capability have made their implementation more attractive in recent years.

Future Work

A recurring issue throughout this campaign was thermal degradation of power system components. The thermal degradation issues seen in this campaign had also occurred during prior campaigns; this was a known issue. Though this was remedied in the last few weeks of the campaign, greater care should be taken to ensure that in selecting components for the thruster's initial design, no materials contained within connectors and other critical components are incapable of withstanding the expected thermal load to be experienced by the thruster throughout sustained operation. A more detailed thermal FEM analysis of the thruster in a multi-physics software application would have been particularly informative prior to starting testing. The new thermal standoff design functions well, but it was only after several weeks of testing that it was implemented.

An additional mechanical design constraint to be considered in future ECR thruster designs featuring antennas is the rate of erosion of the antenna material due to heating. On several occasions, due to the repeated heating and erosion of the antenna at the boron nitride liner interface, the diameter of the antenna at the interface with the boron nitride channel liner became smaller over time. Though the exact physical mechanism that triggered this outcome was not fully characterized, as no video of the phenomenon occurring was captured, after repeated testing, the antenna tended to eject azimuthally from the thruster into the vacuum chamber. Prior to each test, antenna seating into the TNC connector was thoroughly checked. Whether it was a combination of this gradual decrease in diameter over time, some fluid effect of the radially injected propellant being redirected outward and entraining the antenna, or an otherwise uncharacterized electromagnetic effect on the graphite, the resulting effect was that antenna ejection occurred.

To remedy this issue, a PTFE gasket had been designed to attempt to keep the antenna in place, but did not appear to be sufficiently tight to have the intended effect on retaining the antenna. For a future design implementing a graphite antenna, a small O-ring consisting of very heat resistant and plasma-safe dielectric material in radial tension on the antenna would likely be sufficient to prevent this from occurring.

With the redesigned antenna connector and thermal standoff, the interface between the tungsten electrode and graphite antenna proved challenging to work with. A boron nitride standoff contained the electrode-antenna interface. The tungsten electrode featured a 45° cut matching with a 45° cut made on the antenna to increase the contact surface area between these two components for a better friction fit. The primary issue with this design was that as the antenna was slid into the boron nitride standoff, boron nitride powder tended to accumulate at the electrode-antenna interface, increasing the resistance at this point and leading to unintended heating throughout testing.

To avoid this, in a future coaxially-driven ECR design, a fully tungsten antenna could be implemented, thereby eliminating this source of impedance mismatch-driven issues throughout the thruster's power circuit. Given tungsten's higher secondary electron emission characteristics relative to graphite, this modification could prove favorable in triggering higher ionization within the ECR region due to the increase of free electrons available to trigger ionization avalanches. However, it should also be noted that tungsten tends to sputter more than graphite. Careful consideration of the thruster's operating conditions should therefore be made to ensure that if a tungsten antenna were implemented, sputtering would be minimized.

After the thruster showed increased performance at high steady state power settings in excess of 300 W, future testing of this particular thruster design could include characterization in the near range to this power, up to 450 W, the maximum the Sairem GMS450 RF power supply can generate. The only tests completed at or exceeding 300 W at any point in the thruster's operation during this campaign were under steady state operating conditions. The thruster efficiency in excess of 5% at 300 W was particularly promising, and capturing the thruster's performance at this power level under a pulsed regime would be of similar interest.

Beyond the thruster evaluated during this campaign, future work for this project includes the development of a new, fully waveguide-driven thruster. This will eliminate the need for an antenna and its associated connectors, thereby eliminating this design's primary failure points. This high-power thruster will be capable of demonstrating performance over a much wider range of microwave power settings, up to 12 kW. The lessons learned from this campaign have ensured that future test campaigns will avoid many of the same failure modes and bottlenecks that were experienced throughout the testing of the low power thruster. However, it is certain that other failure modes will be discovered.

Throughout this test campaign, high-power performance had largely been limited by the RF power supply available for testing, while future campaigns with the new waveguide thruster will involve the implementation of the aforementioned kW-level power supply. This will enable a significantly larger range of maximum and minimum power settings to be tested, which will potentially unlock additional performance improvements associated with exciting the plasma to a significantly higher energy state during a pulse, with many more energetic, free electrons being available to drive further ionization during minimum power portions of a pulse cycle, potentially minimizing the need for an extended pulse to maintain comparable or improved performance relative to continuous operation.

References

[1] E. Choueiri, "A Critical History of Electric Propulsion: The First Fifty Years (1906-1956)," *Journal of Propulsion and Power,* 2004.

[2] K. Tsiolkovsky, "Study of Outer Space by Reaction Devices, Translation of "Isseldovaniye mirovykh prostranstv reaktivnymi priborami"," "Mashinotroyeniye" Press, Moscow, 1967.

[3] E. Choueiri, "A Critical History of Electric Propulsion Part II: 1957-1979," International Electric Propulsion Conference, London, 2025.

[4] V. Désangles, D. Packan, J. Jarrige and P. Dietz, "ECRA thruster advances: 30W and 200W prototypes latest performances," in *Intenrational Electric Propulsion Conference*, Boston, 2022.

[5] A. J. Sheppard, "Theoretical and Experimental Performance of an Electron Cyclotron Resonance Thruster Operating on Water Vapor Propellant," Seattle, 2021.

[6] T. Vialis, J. Jarrige, A. Aanesland and D. Packan, "Direct thrust measurement of an electron cyclotron resonance plasma thruster.," *Journal of Propulsion and Power,* vol. 34, no. 5, 2018.

[7] B. A. Jorns and B. N. Wachs, "Sub-millinewton thrust stand and wireless power coupler for microwave-powered small satellite thrusters," *Review of Scientific Instruments,* vol. 93, no. 8, 2022.

[8] A. Beresnyak, Plasma Formulary, Washington, D.C.: U.S. Naval Research Laboratory, 2023.

[9] Boni and et al., "A sheath correction method for electron density measurements with the microwave resonant curling probe," *Plasma Sources Science and Technology,* vol. 32, 2023.

[10] T. H. Stix, The Theory of Plasma Waves, New York: McGraw-Hill, 1962.

[11] C. A. Balanis, Antenna Theory: Analysis and Design, Hoboken: John Wiley & Sons, 2005.

[12] K. Wiesemann, "A Short Introduction to Plasma Physics," CAS-CERN Accelerator School: Ion Sources, Senec, 2012.

[13] T. Thuillier, "CERN Accelerator School 2012: Electron Cyclotron Resonance Ion Sources - I," 2012. [Online]. Available: https://indico.cern.ch/event/150974/contributions/195732/attachments/154293/218365/ECR_Ion_Source_I.pdf. [Accessed 2026].

[14] Jarrige and et al., "Performance Comparison of an ECR Plasma Thruster using Argon and Xenon as Propellant Gas," in *International Electric Propulsion Conference*, Washington, D.C., 2013.

[15] U. Shumlak, *Aerospace Plasmas Course Notes,* Seattle, 2023.

[16] P. Thoreau, "Advanced Techniques for Hall Thruster Research and Development," University of Washington, Seattle, 2025.

[17] P. Thoreau, "Development of the SPACE Lab Thrust Stand for Millinewton Thrust Measurement," in *International Electric Propulsion Conference*, 2019, 2019.

[18] R. Hofer, M. Walker and A. Gallimore, "A Comparison of Nude and Collimated Faraday Probes for Use with Hall Thrusters," in *International Electric Propulsion Conference*, Pasadena, 2001.

[19] B. H. Diamond, *Opto-isolated Differential Trans-impedance Amplifier for Faraday Probes,* Seattle: SPACE Lab Faraday Probe Guidelines, 2026.

[20] Maystrenko and et al., "Development of a high dynamic range retarding potential analyzer for electric propulsion plume diagnosis," *Review of Scientific Instruments,* vol. 93, no. 7, 2022.

[21] S. Peterschmitt, "Development of a Stable and Efficient Electron Cyclotron Resonance Thruster with Magnetic Nozzle," Institut Polytechnique de Paris, Paris, 2020.

[22] D. L. Brown and A. D. Gilmore, "Evaluation of Plume Divergence and Facility Effects on Far-Field Faraday Probe Current Density Profiles," in *31st International Electric Propulsion Conferenc*, Ann Arbor, 2009.

[23] J. Emsley, The Elements, Oxford Chemistry Guides, New York City: Oxford University Press, 1995.

[24] J. Frieman, N. Brown, C. Liu, T. Liu, M. Walker, V. Khayms and D. King, "Electrical Facility Effects on Faraday Probe Measurements," *Journal of Propulsion and Power,* vol. 34, no. 1, pp. 267-269, 2018.